Impact of finite element idealisation on the prediction of welded fuselage stiffened panel buckling

Published in:

Document Version:
Peer reviewed version

Queen's University Belfast - Research Portal:
[Link to publication record in Queen's University Belfast Research Portal](#)

Publisher rights

General rights

Take down policy

Impact of Finite Element Idealisation on the Prediction of Welded Fuselage Stiffened Panel Buckling

T. Ekmekyapar[a,*], A. Murphy[b] , D. Quinn[b] and M. Özakça[a]

[a] *Engineering Mechanics Division, University of Gaziantep, 27310 Gaziantep, Turkey*
[b] *School of Mechanical and Aerospace Engineering, Queen's University Belfast, Belfast, N. Ireland, U.K.*

Abstract: Lap joints are widely used in the manufacture of stiffened panels and influence local panel sub-component stability, defining buckling unit dimensions and boundary conditions. Using the Finite Element method it is possible to model joints in great detail and predict panel buckling behaviour with accuracy. However, when modelling large panel structures such detailed analysis becomes computationally expensive. Moreover, the impact of local behaviour on global panel performance may reduce as the scale of the modelled structure increases. Thus this study presents coupled computational and experimental analysis, aimed at developing relationships between modelling fidelity and the size of the modelled structure, when the global static load to cause initial buckling is the required analysis output. Small, medium and large specimens representing welded lap-joined fuselage panel structure are examined. Two element types, shell and solid-shell, are employed to model each specimen, highlighting the impact of idealisation on the prediction of welded stiffened panel initial skin buckling.

[*]**Corresponding author:** Talha Ekmekyapar (E-mail address: ekmekyapar@gantep.edu.tr)

1. Introduction

Lap joints are widely employed in aerospace stiffened panels to assemble the skin and stiffener sub-components together. The assembled panels are required to resist in-service loading conditions without loss of joint integrity for a successful structural design. For large zones of aircraft structure, for example the lower fuselage or upper wing, the extreme loading is compressive and the buckling collapse performance of the panel governs structural design. What is more to increase structural efficiency for panels in insensitive aerodynamic zones, for example elements of the rear fuselage, panels may be designed so that local skin buckling between the stiffeners occurs below the ultimate collapse load. Thus for 'post-buckling' panels, initial skin buckling and panel collapse are key static strength characteristics which must be calculated. These panel stability characteristics are strongly influenced by initial geometric imperfections [1], typically exhibited in a structure due to sub-component manufacturing and panel assembly processes.

To determine the initial buckling, post-buckling and collapse response of a stiffened panel empirical and semi-empirical design formula [2-4] or the Finite Element (FE) method, employing non-linear material and geometric analysis procedures may be used [5-9]. The design formulas rely on applying simplifying assumptions, modelling the panel structure as a series of plates and columns. Using the FE method it is possible to model panel joints in great detail and predict panel behaviour under loading with a high level of accuracy. However, when modelling large wing and fuselage panel structures such detailed analysis becomes computationally expensive. Moreover, when modelling large structures the impact of local joint behaviour on global static strength performance may be weakened, creating a link between appropriate panel and joint idealisation and the size of the modelled panel structure. Thus this study presents coupled computational and experimental analysis, aimed at

developing modelling guidelines for lap joined stiffened panel structure which accounts for the size of the structure being modelled. Three varying size panel structures, representing lap-joined fuselage panels, are investigated. Two levels of modelling fidelity are employed to model each panel specimen with the analysis results used to develop idealisation guidelines.

The article is organised as follows: the first section briefly summarizes key background literature. The following sections then detail the validating experimental work, present the computational analysis of the experimental specimens and document the results from the coupled computational and experimental analysis. The final section concludes the work with a summary of the developed idealisation guidelines

2. Background

There has been a significant volume of research on the modelling of stiffened panel buckling and collapse behaviour. A vast range of analysis methods are available, including Finite Strip [10-12] and Finite Element [5-9]. Focusing on FE analysis, the analysis method to be used herein, recent examples which demonstrate the current state-of-the-art include studies which examine the influence of manufacturing assembly methods on panel strength, for both marine [13-14] and aerospace structures [15-18]. Further examples demonstrate analysis to understand the impact of panel configuration on buckling and post-buckling behaviour [19-20], and the development of efficient design rules for specific panel configurations [21-22].

Further focusing on literature which specifically considers the modelling of lap joined stiffened panels, Lynch et al. [7] and Murphy et al. [8] examine single and multi stiffener fuselage panels under compression and shear loading. Each panel is manufactured using riveted lap joints, with the specimens modelled using shell elements to predict ultimate

collapse loads. The computational analysis indicates the impact of joint idealisation can be significantly greater for small single stiffener panels [7] than for larger multi stiffener panel structures [7-8]. However the individual paper conclusions relating to idealisation do not reference the size or the extent of joints within the modelled panel structure.

Welding is a novel and promising technology for aircraft wing and fuselage assembly processes. Especially the Friction Stir Welding (FSW) process has superior performance compared to other types of welding. It has the ability to weld alloys that are difficult to weld and allows the creation of both butt and lap joints [23]. FSW also has the potential to significantly reduce some undesirable welding effects such as high residual stresses and distortions derived from material melting which occurs in traditional welding processes [24]. Recent work has examined the compression performance of integral wing stiffened panels assembled using FSW butt joints through numerical analysis [18, 25]. Research by Murphy et al. [26] has expanded on this knowledge using numerical and experimental studies, attempting to characterize the impact of individual welding process effects on panel behaviour under compression loading.

Considering welded panels with lap joints, Murphy et al. [15-17] examine initial buckling and collapse of Friction Stir Welded (FSW) stiffened panels under compression loading. In this work the computational and accompanying experimental analysis examines the impact of varying welding effects on panel initial skin buckling and ultimate collapse loads. The computational analysis indicates that the impact of joint and weld effect idealisation can be significantly different for small single stiffener panels [15] and larger multi stiffener panel structures [16-17]. Here again the individual paper conclusions drawn from the work on joint

and weld effect idealisation do not reference the size of the modelled panel structure or the extent of joints within the structure.

Clearly significant knowledge exists on FE modelling of stiffened panels to predict buckling and post-buckling behaviour. However, there exists limited literature and guidance on selecting an appropriate panel idealisation with consideration of the size of the stiffened panel to be modelled. A further worthy note is that only a small number of the available studies consider initial skin buckling. When considering panels assembled with lap joints the selected joint idealisation directly impacts the outer dimensions of any buckling unit and creates the buckling unit edge boundary conditions. Thus panels assembled with lap joints and designed to function within the post-buckling domain may be particularly sensitive to joint idealisation and thus particularly appropriate for investigation.

3. Panel experimental analysis

To develop relationships between panel idealisation and the size of the modelled panel structure three coupled experimental and simulation case studies are presented. Each case study considers a similar panel design but a different size specimen, with each having validating experimental results to benchmark the simulation predicted static strength behaviour. Three panel specimen designs already available in the literature are examined [15-17]. Each design is representative of compression critical aircraft fuselage structure. The panel specimen designs are presented in Figure 1 and Table 1. The smallest specimen consists of a single longitudinal stiffener plus attached skin (S1) [15], the middle size specimen consists of three longitudinal stiffeners (S3) [16] and the largest specimen consists of five longitudinal and two lateral stiffeners (S7) [17].

Each specimen was manufactured using standard aerospace materials (stiffeners AA7075 extrusions, skin AA2024 sheet). The longitudinal stiffeners of specimens S1 and S3 were assembled to the skin using FSW. The central three longitudinal stiffeners for specimens S7 were assembled to the skin using FSW, with the edge longitudinal stiffeners and the lateral stiffeners assembled to the welded skin-stiffener structure using standard aerospace countersunk rivets and a standard manual riveting process. Each specimen was tested under uniform compression loading. Before testing the specimen ends were cast in cerrobend or epoxy tooling resin, allowing simultaneously the uniform compression loading of the specimens and clamped loading edge boundary conditions. During the tests specimen loading, end-shortening and strain data from key specimen locations were recorded at short load intervals.

For all specimens additional supplementary measurements and tests were undertaken to determine the basic specimen material properties. As the specimens were welded further experimental measurements were undertaken to capture the size of the degraded material zone around the weld joint (typically called the Heat Affected Zone – HAZ), and its associated material properties. In order to understand the residual stress magnitudes present within the specimen a series of measurements via the hole-drilling method [27] were performed on similar scale specimens which were fabricated from the same batch of materials and using the same welding process parameters. These measurements along with welding process FE simulations were used to approximate the residual stress state present within the tested specimens. Further information on the case study specimens, individual test setups and experimental results can be found in the individual references [15, 16, 17].

4. Panel computational analysis

For any analysis the structure must be idealised with appreciation of the possible structural behaviour as the computational model must accurately represent such behaviour. Optimised stiffened panels are susceptible to local skin and stiffener buckling behaviour as well as global stiffener buckling behaviour. An appropriate idealisation is therefore to represent the stiffener individual web and flange components along with the panel skin as an assemblage of shell or solid elements [5]. This approach is essential to enable both the local and global buckling modes of the structure to be predicted. In the literature the vast majority of preceding works have used shell elements [5-9, 13-17], generating acceptable panel strength predictions. Herein each case study specimen will be modelled twice, in the first instance using the well practised shell element idealisation, and then using the more novel solid-shell element idealisation. For each case study and each idealisation the accuracy of the predicted panel static strength performance along with the computational expense of the analysis will be presented and analysed, thus enabling the advantages and disadvantages of both element type idealisations to be understood. Solid elements are not considered in the study as they would naturally result in either poor aspect ratio elements and potentially poor/inappropriate predictions, or a significantly large number of elements with appropriate aspect ratios but with a simulation that would be very costly to build, run, post-process and store.

Modelling with the two structural element types the local idealisation of the skin-stiffener lap joints may be modelled with two unique high fidelity idealisations. In the shell model rigid link MultiPoint Constraints (MPCs) [28] are used to represent the connected zones (that is to say the panel stiffener and skin zones which have been welded together (Figure 2), and in addition for specimen S7 the panel zones which represent where edge stiffeners have been riveted to the panel skin (Figure 1)) of the skin-stiffener interfaces. The remaining interface

zones are modelled using contact gap elements. To represent the connected zones of the skin-stiffener interfaces in the solid-shell element models, the upper nodes of the panel skin and the lower nodes of the stiffener flanges are merged along all weld lines, Figure 2. For the solid-shell model of specimen S7 merging is also done along all rivet lines joining the skin to the edge stiffeners. In the remaining interface zones surface to surface contact elements are used. Figure 2 depicts a schematic of the two local lap joint idealisations. The shell elements are located at the mid-plane thickness of each segment of specimen skin, web or flange. Using solid-shell elements there is no need for such mid-plane idealisation. The total model cross-sectional area of both FE models is equal and corresponds exactly to the individual test specimen cross-sectional areas.

For any FE analysis an element and mesh convergence study must be performed to determine an appropriate model mesh for a particular element formulation. When examining the buckling collapse behaviour of stiffened panels the aim is the definition of the minimum mesh density required to accurately represent the structures possible buckling waveforms. Based on a series of element and mesh convergence studies, which examined the buckling behaviour of rectangular plates with geometries and boundary conditions designed to represent those of specimen individual skin, flange and web units, appropriate element formulations and mesh densities were initially defined. This preliminary analysis employed the element selection and mesh convergence procedures outlined in Murphy et al. [29], generating comparable results with those presented within the reference. For the shell models a four noded element, Shell181 [28], with six degrees of freedom at each node along with a mesh density of the order of 5.0 mm (Figure 3-5) was determined most appropriate for this study. To represent contact and sliding at the shell model skin-stiffener interfaces a two noded contact element, Conta178 [28], with three degrees of freedom at each node was

coupled with the developed shell mesh. For the solid-shell models an element with continuum solid element topology and featuring eight node connectivity with three degrees of freedom at each node, Solsh190 [28], was found most appropriate. For the solid-shell models an identical mesh to the shell models was determined most appropriate for this study (Figure 3-5) along with Conta173 and Target170 elements [28] selected to represent panel interface contact.

Shell181 and Solsh190 elements are suitable for analysing thin to moderately thick shell structures and well suited for non-linear applications [28]. Also, the formulations of both elements are based on logarithmic strain and true stress. In the element domain by default Shell181 uses a reduced integration scheme for improved performance. The default number of integration points through the thickness is three; however when plasticity is present the number of integration points is changed to be five. On the other hand, unlike shell elements, Solsh190 is fully compatible with 3-D constitutive relations and has the continuum solid element topology. Moreover, the Solsh190 element uses two integration points through the thickness by default. In order to alleviate shear locking both elements utilize the assumed strain method. Moreover the Solsh190 element employs an enhanced strain formulation to improve in-plane bending behaviour [28]. Although both elements allow modification to their formulation properties, no effort was made to change default parameters.

Material curves were incorporated into the simulations using a multi-linear isotropic strain hardening material model [28]. Skin and stiffener material properties were generated experimentally using coupons taken from the same material batches used for specimen manufacture. Specimen weld degraded material properties were also experimentally determined and again incorporated into the simulations using a multi-linear isotropic strain

hardening material model. Lynch et al. [7] outlines the detailed procedures used for testing the material coupons and Murphy et al. [16] defines the detailed procedures used to process the test data for inclusion within the FE simulations.

As initial geometric imperfections can lead to widely varying initial buckling and collapse behaviour great care was taken when generating initial imperfections. In considering the case study specimen design and manufacture, the main source of specimen geometric imperfections results from the thermal and mechanical stresses developed during the welding assembly processes. Using the FE method it is possible to represent weld induced geometric imperfections [17]. To do so, a simplified residual stress state is introduced into an initial FE model of the as-designed perfect specimen structure. When the residual stresses are introduced to the model, the structure is no longer in equilibrium, and a non-linear geometric analysis is carried out to establish static equilibrium. The equilibrium calculation generates a distorted structure, and a slightly modified stress state. This step represents the unclamping of the assembled structure from any fixturing required during the welding process [30]. A second stage simulation is then required to represent additional manufacturing processes, for example attaching the riveted stiffeners of specimen S7 and test preparation processes such as clamping and casting specimen ends. To model these processes the stressed and deformed mesh output of the first analysis has appropriate nodes (for example the skin nodes along rivet lines or the skin nodes within clamped and cast areas) displaced back to a zero out-of-plane location before a second non-linear geometric analysis is carried out to establish static equilibrium.

An initial state command, INISTATE [28], is used to define the initial stress state in both model types. For each specimen the same magnitude of stress is applied over the same

volume of specimen material for each idealisation. Table 2 presents the longitudinal and lateral tension stress magnitudes and their application areas for each specimen. Applying a single approach to generate specimen imperfections will enable the assessment of panel size on the prediction of buckling for each model type (shell and solid-shell) when applying a single simulation route. However, interpreting and comparing the predictions between model types (shell and solid-shell) will be more challenging as the element type will influence the predicted geometric imperfections and the element type along with the predicted imperfections will in combination influence the panel strength behaviour. Care must therefore be taken when comparing predicted buckling behaviour between the two model types (shell and solid-shell) if their predicted imperfections are significantly different. Further detail on the applied approach used to introduce the residual stress state into the models is available in reference 17. Assessment of simulation strength prediction accuracy using this approach is also available for a range of panel geometries [17, 26]. Figure 6 illustrates a flow diagram of the FE analysis steps undertaken to include the residual stress based imperfections within the simulation models.

Having created an imperfect specimen model a final analysis is performed representing the compression test. The analysis applies the test loads and boundary conditions to the imperfect model, Figure 6. To represent specimen loading, a uniform axial displacement is applied to the nodes at the lower end of the model, while the axial displacement of the nodes at the opposite end of the model are restrained in the same direction. To represent the specimen cast ends and the stiffener flanges which are constrained within edge guides during test (specimen S7), the out-of-plane displacements of the nodes within these zones are restrained. For the shell models each mid-plane node in the boundary condition zone is constrained against out-of-plane displacement. Rotations are not constrained at the individual nodes, matching the

test conditions, however as there are multiple nodes in each zone the individual node out-of-plane constraints combine to constrain specimen rotations, again matching the real test conditions. Considering the solid-shell models, the nodes through the thickness of the skin, web or flange are constrained from out-of-plane displacements resulting in the same effect on specimen rotations. However as the out-of-plane constraints are applied at multiple nodes through the thickness an additional constraint is applied to the solid-shell models (compared to the shell model with only one node through the thickness). As multiple adjacent longitudinal and lateral nodes are restrained within all the cast and edge guide zones the impact on the specimen behaviour due to two slightly different boundary conditions may be hard to quantify. Were a greater impact may be seen is in the modelling of the lateral stiffeners of specimen S7. Experimentally the lateral stiffeners were constrained from out-of-plane displacements using a series of tie rods connected from the lateral stiffeners to remote anchor points [17]. In the simulations the lateral stiffeners are not modelled but represented using displacement boundary conditions. Within the shell models the skin nodes along the lateral stiffener rivet lines are constrained from out-of-plane displacements. To represent the lateral stiffeners within the solid-shell models all nodes through the skin thickness along the rivet lines are constrained from out-of-plane displacements. In this case the different boundary conditions will impact on panel behaviour as only a single line of multiple adjacent lateral nodes are restrained from out-of-plane displacements, resulting in different levels of rotational constraint about the lateral rivet lines. Thus when examining the simulation results for S7 it will be important to recognise that the shell and solid-shell models have different lateral stiffener boundary conditions and that both are approximate idealisations of the real experimental setup. Figure 7 illustrates the boundary conditions applied in the present study.

For all simulation stages a displacement controlled incremental-iterative Newton-Raphson solution procedure was used [31]. During the implicit FE analysis the end-shortening load is applied monotonically in small increments representing the test conditions. During loading the instability of the skin develops depending on the initial imperfection pattern across the skin segments, and with marginally different initial conditions at different locations marginally different buckling loads will be calculated. Where possible to allow direct comparison between the experimental and computational results initial skin buckling is determined using the average strain method [32]. The method plots the load against the mid-plane strain at a selected location, with initial buckling defined to have occurred when a sharp break is seen in the data. Based on early simulation observations in which a range of initial buckling locations where observed a number of locations were selected to calculate initial buckling for each specimen. A total of six locations are examined for specimen S1, ten locations for S3 and fourteen locations for S7, Figure 1. For specimen S7 initial buckling is expected within the specimen central zone as the test boundary conditions stabilise the outer skin bays. Finally, the ultimate specimen collapse load is defined as the maximum experimental or computational load carried by the specimen or model.

5. Experimental and simulation results

5.1 Specimen S1

The performance of three test specimens is presented in reference 15, with one instrumented to capture initial skin buckling behaviour. This specimen experienced initial skin buckling at 16.6 kN and failed in a crippling mode at 71.7 kN. The skin buckling load was calculated using strain gauge data from location P5, see Figure 1. The specimen skin segments initially buckled into single longitudinal half-waves before changing mode into two longitudinal half-waves at 48.0 kN. At specimen collapse the skin segments rotated in the opposite direction to

the stiffener web and free flange just below the mid-plane of the specimen. The specimen skin-stiffener weld remained intact up to and during specimen collapse. Figure 8 presents the measured load versus end-shortening curve. The results of the FE analyses will be discussed next. The figure also presents a final test image of the specimen at which stage the weld joint has failed due to post collapse end-shortening of the specimen.

Considering the simulation predicted behaviour, Figure 9 presents the initial specimen geometric imperfection patterns induced by modelling the idealised welding residual stress state. Figure 10 presents the key magnitudes of the geometric imperfections once the test boundary conditions have been applied to the models. The simulations predict the same imperfection pattern with the shell model predicting marginally larger magnitudes. This highlights the potential impact of the two element type boundary condition idealisations, with the shell model only having the single mid-plane nodes constrained against out-of-plane displacements but the solid-shell models having at least two nodes through the thickness of the skin, web or flange constrained from out-of-plane displacements. Unfortunately for this specimen there is no experimental geometric imperfection data available. However if we examine the initial axial stiffness data in Figure 8 the solid-shell model predicts a 16.7% greater stiffness and the shell model a 12.8% greater stiffness than that measured during experimental specimen test. This suggests that the real specimen imperfection is larger in magnitude than that generated by the idealised residual stress state.

The simulation predicted initial skin buckling loads are presented in Table 3. Both simulations predict initial asymmetric skin segment buckling with two longitudinal half-waves, however the initial buckle waves of the shell and solid-shell models are in opposite directions, Figure 8. The shell model initially buckles at 17.5 kN at location P5, and the solid-

shell model initially buckles at 16.2 kN at location P4. Unexpectedly, the shell model buckling loads are greater in magnitude despite greater geometric imperfection magnitudes and the less heavily constrained cast end boundary conditions.

Comparing the minimum and maximum predicted skin buckling loads for different points within each model the range of calculated buckling loads for the shell model is marginally larger (13.1%) than that predicted by the solid-shell model (9.3%). This highlights the importance of location when calculating and comparing buckling behaviour. Variation in the predicted buckling load at a single location ranges from 1.1% at location P1 to 11.1% at location P3.

Figure 11 presents average strain data at the six buckling calculation locations defined in Figure 1. It is evident from the strain data that the solid-shell model predicts a skin mode change at 32.7 kN, this results in a single longitudinal half-wave within each specimen skin segment, Figure 8. It is worth noting that it is not possible to detect this mode change in the predicted load versus end-shortening curve.

The collapse load predictions are 68.5 kN and 73.3 kN for the shell model and the solid-shell model respectively. The shell model predicts a very similar collapse mode to the experimental behaviour, under predicting the experimental collapse load by 4.5%. The solid-shell model predicts a different collapse mode and a higher collapse load (2.2%) than that measured experimentally. The mode change identified within the average strain data of the solid-shell model results in increased skin and stiffener flange buckle wave-lengths and ultimately this leads to larger skin and flange buckle-waves at specimen collapse, which was not seen in the physical testing.

Examining the computational cost, the solid-shell model took approximately 3.56 times longer to reach maximum load than the shell model. Also it is worth noting that the shell model experienced convergence difficulties after reaching the maximum load and could not achieve the ultimate target end-shortening of 1.6 mm. The solid-shell model experienced no such difficulty.

In order to assess the impact of boundary conditions on simulation predictions a brief boundary condition sensitivity analyses is also undertaken employing a shell element model. Considering specimen S1 three different models are built and simulation results assessed against the available test results. The three boundary conditions considered are:

- simple supported loaded edges (the nodes at the lower and upper ends are simply supported),

- fixed loaded edges (the nodes at the lower and upper ends are clamped – rotations constrained),

- and the test boundary conditions (this represents the boundary conditions employed through the paper).

These different boundary conditions lead to major differences in the response of the panel, as shown in Figure 12. The post-buckling and failure behaviours change due to the applied location of the boundary conditions and the form of the constraints, Figure 12. Given the similarity between the experimental buckling and collapse behaviour and that predicted by the model with the test boundary condition – a solid level of confidence is generated in the applied modelling approach. However it is worth remembering the model boundary conditions can have significant impact on the predicted numerical results.

5.2 Specimen S3

The skin buckling load of specimen S3 was calculated to be 21.5 kN using strain gauge data from location P8, see Figure 1. The skin bays buckled with five approximately equal length half-waves with almost the equivalent asymmetric pattern in each bay. However, in one of the skin bays two of the buckle half-waves, in the region of P1 and P2, combined into a single half-wave. Specimen failure was measured at a load of 166.4 kN with the central stiffener buckling with combined global flexure and local stiffener flange and web buckling. Figure 13 presents the measured load versus end-shortening curve for specimen S3.

Figure 14 presents the predicted initial specimen geometric imperfection patterns induced by modelling the idealised welding residual stress state and Figure 15 presents the imperfection magnitudes once the test boundary conditions have been applied to the models. The simulations predict the same imperfection pattern with again the shell model predicting marginally larger magnitudes. In this case it is not clear that the different shell and solid-shell cast end boundary conditions are responsible for the magnitude difference. Comparing with the available experimental imperfection data the maximum out-of-plane magnitude of the curvature parallel to the specimen stiffeners (measured from the specimen edge to the specimen centre) was 120% the skin thickness, with the shell model which predicts the larger imperfection having an equivalent imperfection magnitude of only 9.15%. In this case the shell model predicts a 6.3% greater initial specimen stiffness and the solid-shell model a 10.3% greater stiffness than the magnitude measured experimentally. Again this indicates that the real specimen imperfection is larger in magnitude than that generated by the idealised residual stress state.

Table 4 presents the calculated skin buckling loads and Figure 16 presents the interpreted strain data. The models predict very similar skin buckling modes consisting of five half-waves within each skin bay, as shown in Figure 13. The predicted skin buckling modes are similar to the experimental buckling wave pattern except for the combined half-waves located at P1 and P2 as noted earlier. The shell model initially buckles at 23.2 kN calculated at locations P2, P4 and P8, and the solid-shell model initially buckles at 23.2 kN at P8. The maximum variation at a single location is 4.7% (at P7) and for the majority of the skin bay locations the shell model predicts greater or equal skin buckling loads when compared to the solid-shell model predictions. The variation in the predicted buckling loads over the ten sample points for the shell model is 27.2%. As seen in the specimen S1 results the scatter for the solid-shell model is marginally smaller in comparison to the shell model predictions with a 21.6% variation. In general the predicted buckling loads are not as close to the measured experimental behaviour as those predicted for specimen S1.

Examining collapse behaviour both models predict similar central stiffener global flexure and local stiffener flange and web buckling as observed experimentally, Figure 13. The shell model is conservative; predicting collapse 0.4% below the experimental value, the solid-shell model over predicts the experimental collapse load by 4.8%. The predicted collapse loads are closer than those predicted for specimen S1.

In this case the solid-shell model required 3.22 times more CPU time to reach a maximum specimen load when compared with the shell model. Again the Newton-Raphson solution method performs well for the solid-shell model but again convergence issues emerged for the shell model beyond the maximum specimen load.

5.3 Specimen S7

Specimen S7 initially buckles with four approximately equal length half-waves within the specimen central skin bays. The central skin bays buckle with an asymmetric pattern. In this case only strain gauge data is available from a single side of the specimen skin at location P11 (Figure 1) to calculate a buckling load. The extracted load versus strain curve does not have a distinct behaviour to establish an initial buckling load, thus a mathematical curve fitting method was used to determine a buckling load level of 89.7 kN.

For specimen S7 weld joint integrity was maintained through initial skin buckling, post-buckling and overall specimen collapse. The specimen failed at 336.8 kN by combined stiffener global flexure and local free flange instability at the mid-plane of the specimen. Figure 17 presents the measured load versus end-shortening curve plus a post collapse image of the specimen.

Figure 18 presents the predicted initial specimen geometric imperfection patterns induced by modelling the idealised welding residual stress state. Again both modelling approaches predict the same initial geometric imperfection patterns when the idealised welding residual stress state is introduced into the perfect geometry models. However once the lateral stiffeners and test boundary conditions have been applied larger differences in magnitude and the final direction of imperfections is evident, Figure 19. This is primarily due to the imperfection simulation used to represent the attachment of the riveted lateral stiffeners; in which the skin nodes along the lateral stiffener rivet lines are displaced back to their zero out-of-plane location. For the shell model the single mid-plane nodes are displaced back to their zero out-of-plane location, and for the solid-shell model the nodes at the top and the bottom of the skin, through its thickness, are both displaced back to their zero out-of-plane locations.

This enforces reduced longitudinal rotations around the lateral stiffener rivet lines and this significantly impacts the final form of the panel imperfection. There is no experimental geometric imperfection data available for this specimen. However, comparing the initial stiffness predictions of the two FE models and measured test specimen stiffness, Figure 17, the solid-shell model predicts an initial stiffness 1.2% greater than the measured initial stiffness and the shell model predicts an initial stiffness 1.1% less than the measured initial stiffness.

Figure 20 and Table 5 presents the skin buckling behaviour of the two FE models and the experimental specimen. The two FE models predict three longitudinal half-waves within the central specimen bays and two half-waves in the outer bays. The two models predict similar buckling loads, with the shell model predicting initial buckling 3.0% below the experimental value at 87.0 kN (P2-6 and P9-13) and the shell model predicting initial buckling 3.6% below the experimental value at 86.5 kN (P2-6 and P9-13). The variation in skin buckling load predictions between the fourteen analysis locations is 14.9 % and 14.5% for the shell model and the solid-shell model respectively. Variation at a single location between the two models is very small, with a maximum difference of just 1%. In general the predicted buckling loads are closer to the measured experimental behaviour than those predicted for specimen S3. In addition variation in skin buckling load predictions between the analysis locations and at a single location are consistently smaller than that seen for specimen S3.

The employed displacement controlled Newton-Raphson method fails to converge before capturing the collapse of both FE models. Although both FE models fail to converge, the solid-shell model proceeds approximately 10% farther than the shell model. Re-examining the use of the displacement controlled loading conditions. Two of the three test series were

conducted under displacement controlled loading conditions. Hence a displacement controlled loading scheme is appropriate for the simulation studies. Also it can be desirable to see the behaviour of the specimen beyond collapse and such failure paths can be traced using such a solution procedure. However, the conventional force controlled Newton-Raphson method which evaluates displacement increments for a given load step falls short when the tangent stiffness matrix approaches zero. In a force controlled scheme when the limit point is reached the tangent stiffness matrix becomes perpendicular to the external force axis. At this point the tangent stiffness matrix takes a singularity form and convergence cannot be satisfied anymore [33]. This point may represent only a local limit point and beyond this point the structure may be capable of carrying greater load. When using the non-linear stabilisation method artificial dampers are added to the structural system. When buckling occurs large displacements occur over small load steps and the artificial dampers then generate resistive forces to stabilise the problem. Stabilisation can help with convergence problems, but it can also affect accuracy if the stabilisation energy or forces are too large [28]. Herein there are two reasons not to utilise the non-linear stabilization method in the present study. First the current specimen models are very large in terms of degrees of freedom therefore it is very difficult to control the non-linear stabilisation method over these models with an optimum energy dissipation ratio or damping factor. Secondly the models are developed to compare buckling predictions and artificial dampers would change the response of the individual models making comparisons of the two models more difficult.

Examining the solution time, the solid-shell model required 2.84 times more CPU time to reach the maximum converged iteration compared to the shell model.

6. Conclusions

This study examined the relationships between modelling fidelity and the size of the modelled structure, when the global static load to cause initial buckling is the required analysis output. Small, medium and large specimens representing lap-joined fuselage panel structure have been examined. Two element types, shell and solid-shell, have been employed to model each specimen.

- For the examined specimens the predicted initial buckling loads are of a reasonable accuracy compared to the experimental results.

- The variation between shell and solid-shell results appears to decrease with increasing specimen size.

- The scatter in predicted initial buckling loads due to variation in measurement location also decreases with increasing specimen size; however the number and location of the data points are inconsistent between model sizes.

- Element type impacts the format of model boundary conditions which can impact the buckling mode behaviour and thus can impact the predicted buckling loads.

- The solid-shell models appear more robust within the post-buckling regions but are significantly more time consuming to execute.

References

[1]   Paulo RMF, Teixeira-Dias F, Valente RAF. Numerical simulation of aluminium stiffened panels subjected to axial compression: Sensitivity analyses to geometrical imperfections and material properties. Thin-Walled Struct. 2013; 62: 65-74.

[2]   Bruhn EF. Analysis and design of flight vehicle structures. 1st ed. Tri-State Offset Company, 1973.

[3]   NASA, NASA Astronautics structures manual, Volume 3, NASA, Washington, US, 1961.

[4]   Niu MC. Airframe stress analysis and sizing. 2nd ed. Hong Kong Conmilit Press Ltd, 1999.

[5]   Domb MM, Elliott WG, Leigh BR. Modelling of stiffener crippling phenomena using finite element analysis. Canadian Aeronautics and Space Journal 1998; 44: 256-262.

[6]   Hu SZ, Jiang LA. Finite element simulation of the test procedure of stiffened panels, Marine Structures 1998; 11: 75-99.

[7]   Lynch C, Murphy A, Price M, Gibson A. The computational post buckling analysis of fuselage stiffened panels loaded in compression. Thin-Walled Struct. 2004; 42: 1445-1464.

[8]   Murphy A, Price M, Lynch C, Gibson A. The computational post-buckling analysis of fuselage stiffened panels loaded in shear. Thin-Walled Struct. 2005; 43: 1455-1474.

[9]   Campbell J, Hetey L, Vignjevic R. Non-linear idealisation error analysis of metallic stiffened panel loaded in compression. Thin-Walled Struct. 2012; 54: 44-53.

[10] Riks E. Buckling and post-buckling analysis of stiffened panels in wing box structures. International Journal of Solids and Structures 2000; 37: 6795–6824.

[11] Guo YL, Lindner J. Analysis of elastic-plastic interaction buckling of stiffened panels by spline finite strip method. Computers & Structures 1993; 46: 529-536.

[12] Özakça M, Tayşi N, Kolcu F. Buckling optimization of variable thickness prismatic folded plates. Thin-Walled Struct. 2003; 41: 711-730.

[13] Paik JK. Buckling collapse testing of friction stir welded aluminium stiffened plate structures. Report, Ship Structure Committee, 2009.

[14] Khedmati MR, Bayatfar A, Rigo P. Post-buckling behaviour and strength of multi-stiffened aluminium panels under combined axial compression and lateral pressure. Marine Structures 2010; 23: 39-66.

[15] Murphy A, Price M, Curran R, Wang P. The integration of strength and process modeling of friction-stir-welded fuselage panels. AIAA Journal of Aerospace Computing, Information, and Communication 2006; 3: 159–176.

[16] Murphy A, McCune W, Quinn D, Price M. The characterisation of friction stir welding process effects on stiffened panel buckling performance. Thin-Walled Struct. 2007; 45: 339-351.

[17] Murphy A, Ekmekyapar T, Özakça M, Poston K, Moore G, Elliott M. Buckling/post-buckling strength of friction stir welded aircraft stiffened panels. Proceedings of the Institution of Mechanical Engineers Part G, Journal of Aerospace Engineering 2014; 228: 178-192.

[18] Yoon JW, Bray GH, Valente RAF, Childs TER. Buckling analysis for an integrally stiffened panel structure with a friction stir weld. Thin-Walled Struct. 2009; 47: 1608-1622.

[19] Khedmati MR, Ghavami K. A numerical assessment of the buckling/ultimate strength characteristics of stiffened aluminium plates with fixed/floating transverse frames. Thin-Walled Struct. 2009; 47: 1373-1386.

[20] Quinn D, Murphy A, McEwan W, Lemaitre F. Stiffened panel stability behaviour and performance gains with plate prismatic sub-stiffening. Thin-Walled Struct. 2009; 47: 1457-1468.

[21] Hughes OF, Ghosh B, Chen Y. Improved prediction of simultaneous local and overall buckling of stiffened panels. Thin-Walled Struct. 2004; 42: 827-856.

[22] Paik JK. Empirical formulations for predicting the ultimate compressive strength of welded aluminum stiffened panels. Thin-Walled Struct. 2007; 45: 171-184.

[23] Gibson BT, Lammlein DH, Prater TJ, Longhurst WR, Cox CD, Ballun MC, Dharmaraj KJ, Cook GE, Strauss AM. Friction stir welding: Process, automation and control. Journal of Manufacturing Processes. 2014; 16: 56-73.

[24] Paulo RMF, Carlone P, Valente RAF, Teixeira-Dias F, Palazzo GS. Influence of friction stir welding residual stresses on the compressive strength of aluminium alloy plates. Thin-Walled Struct. 2014; 74: 184-190.

[25] Caseiro JF, Valente RAF, Andrade-Campos A, Yoon JW. On the elasto-plastic buckling of Integrally Stiffened Panels (ISP) joined by Friction Stir Welding (FSW): Numerical simulation and optimization algorithms. International Journal of Mechanical Sciences. 2013; 76: 49-59.

[26] Murphy A, Ekmekyapar T, Quinn D, Özakça M, Poston K, Moore G, Niblock J. The influence of assembly friction stir weld location on wing panel static strength. Thin-Walled Struct. 2014; 76: 56-64.

[27] ASTM E837-13. Standard Test Method for Determining Residual Stresses by Hole-Drilling Strain Gage Method. American Society for Testing and Materials. ASTM International, West Conshohocken, PA, United States, 2013.

[28] ANSYS, ANSYS User manual, in, ANSYS Inc., PA, USA.

[29] Murphy A, Price M, Gibson A. Toward virtual testing of airframe stiffened panels. In: Royal Aeronautical Society- Virtual Testing Conference, London, UK, 25-26 October 2006, pp. 1-14.

[30] McCune R, Murphy A, Price M, Butterfield J. The influence of friction stir welding process idealisation on residual stress and distortion predictions for future airframe assembly simulations. Journal of Manufacturing Science and Engineering 2012; 134: 031011.

[31] Becker AA. Understanding non-linear finite element analysis - Through illustrative benchmarks. 1st ed. NAFEMS, 2001.

[32] Singer J, Arbocz J, Weller T. Buckling experiments: Experimental methods in buckling of thin-walled structures. 1st ed. John Wiley & Son, 1997.

[33] Shi J. Computing Critical Points and Secondary Paths in Nonlinear Structural Stability Analysis by the Finite Element Method. Computers and Structures. 1996; 58: 203-220
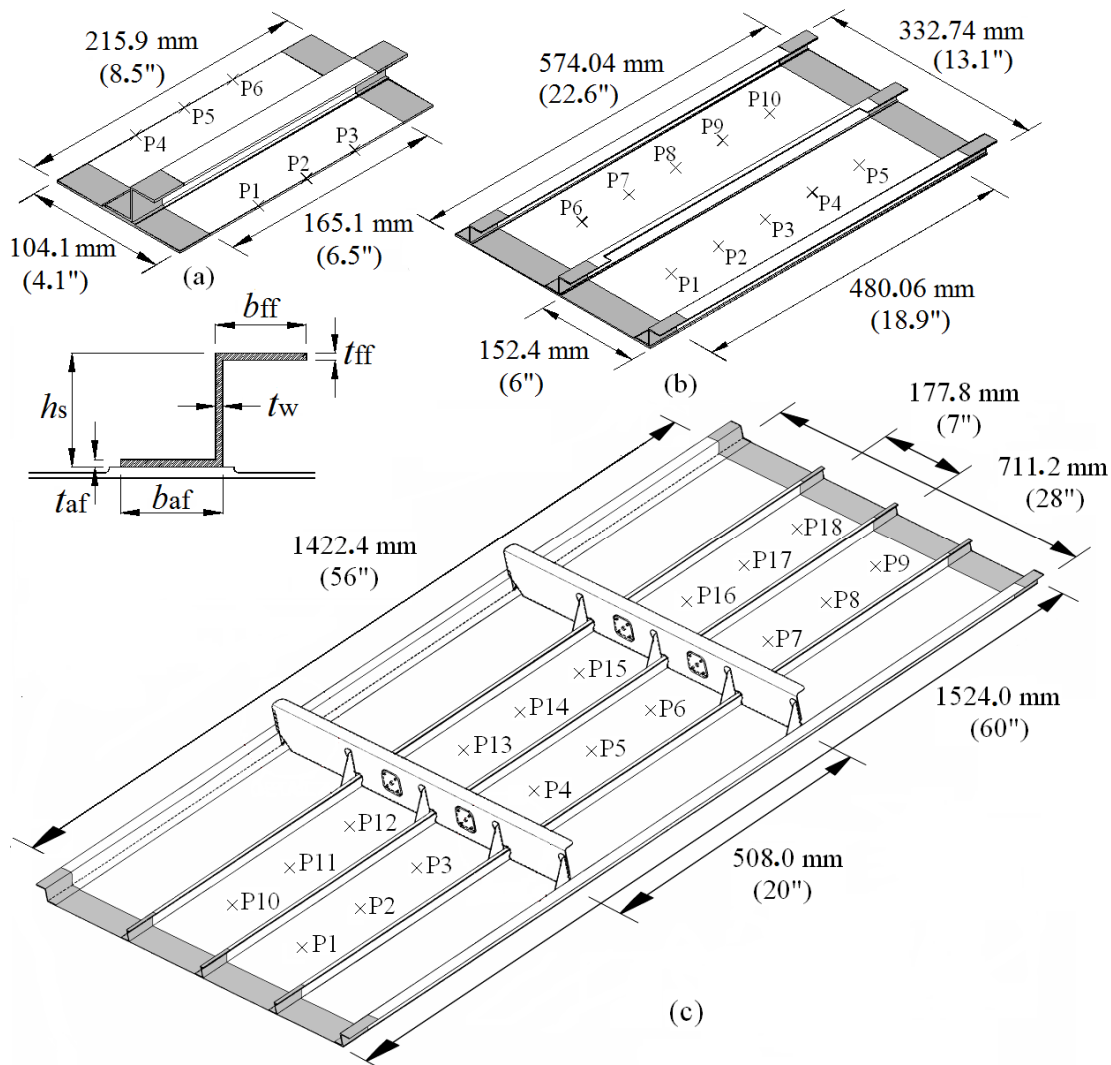
Figure 1. Case study specimen plus locations at which strain data is used to calculate skin buckling.

a) Shell model

b) Solid-Shell model
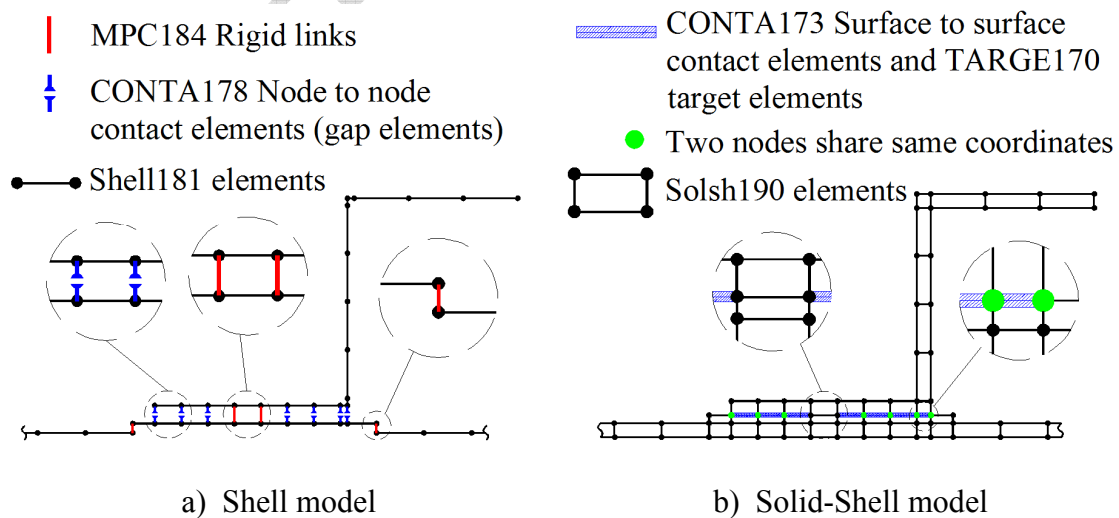
Figure 2. Lap joint idealisations.

a) Shell model   b) Solid-shell model
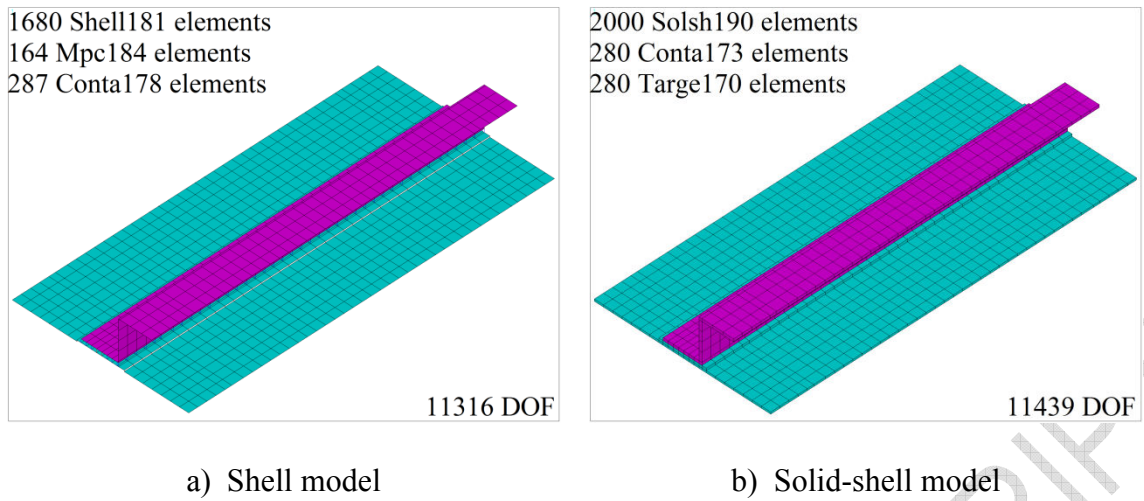
Figure 3. FE mesh for specimen S1.

a) Shell model   b) Solid-shell model
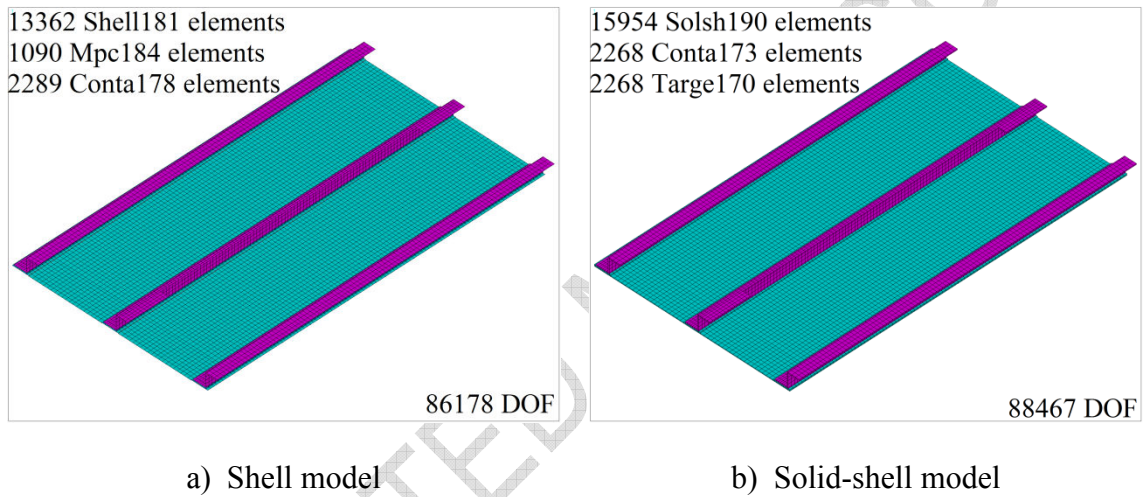
Figure 4. FE mesh for specimen S3.

a) Shell model   b) Solid-shell model
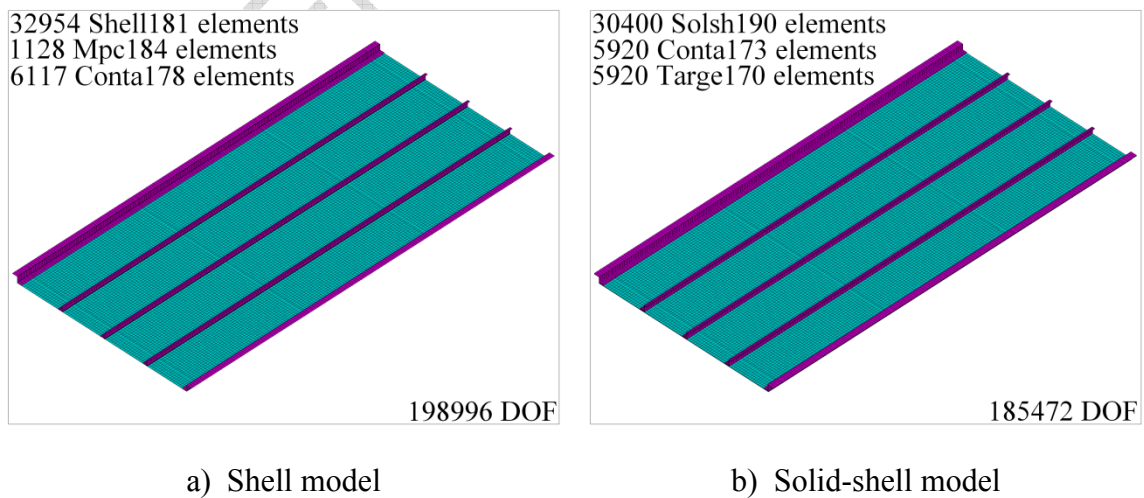
Figure 5. FE mesh for specimen S7.

Build model with perfect geometry and post weld material properties (parent and HAZ material properties)

↓

Introduce a residual stress state to the perfect geometry model

↓

First stage analysis:
Performa non-linear analysis to provide panel equilibrium

↓

Second stage analysis:
Starting with the output of previous stage perform a non-linear analysis to simulate panel clamping and casting processes in preparation to test

↓

Final analysis:
Starting with the output of previous stage perform a non-linear analysis with test boundary conditions applying test loading

Figure 6. Flow diagram of analysis steps undertaken to include a residual stress based imperfection within a simulation model
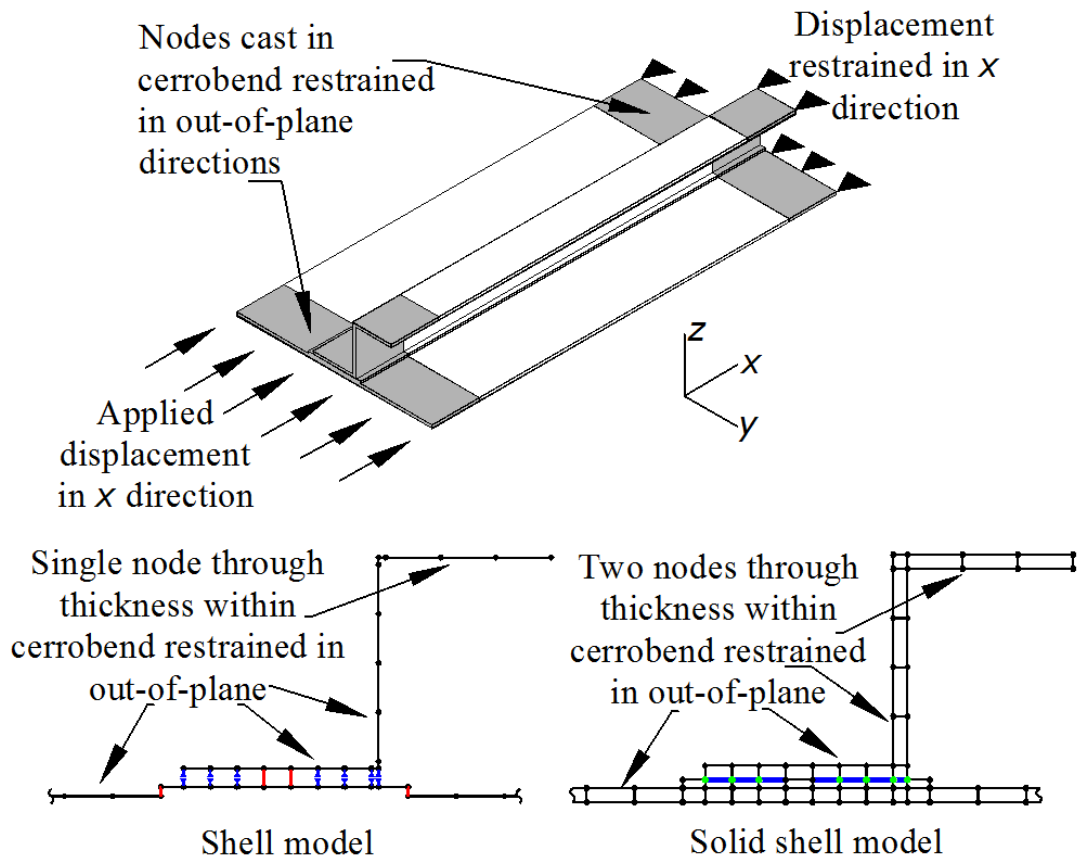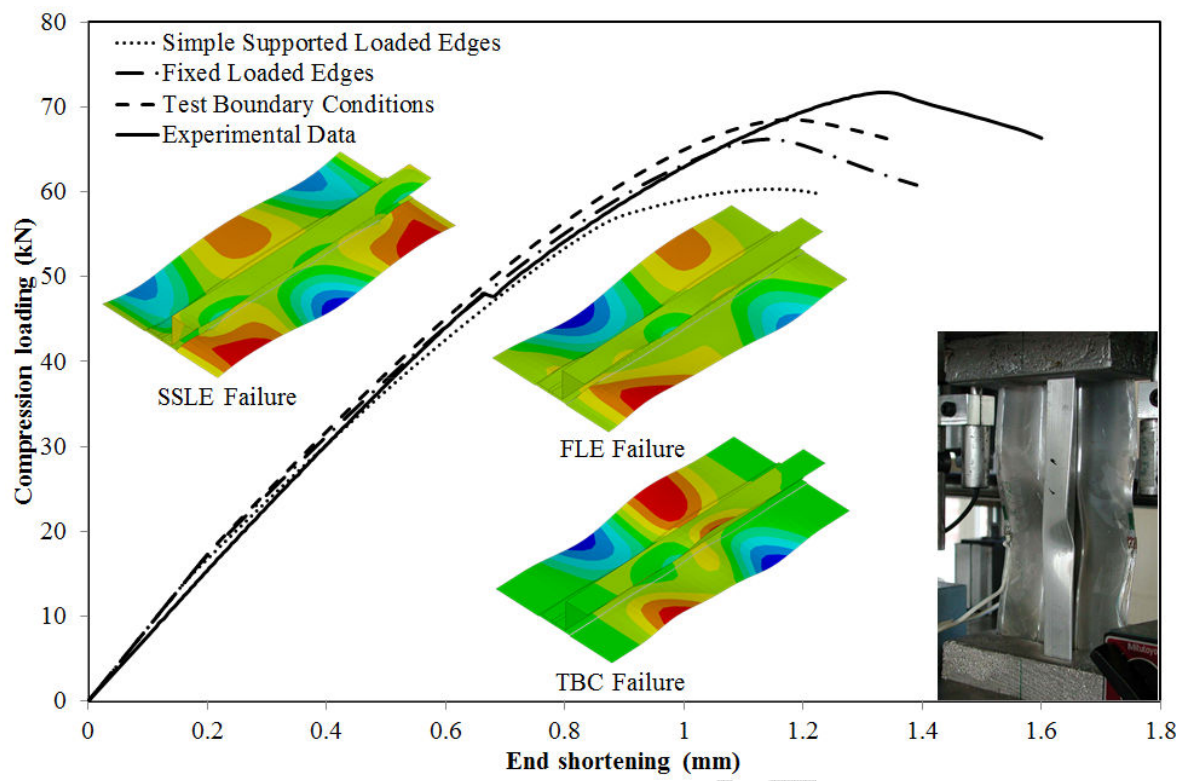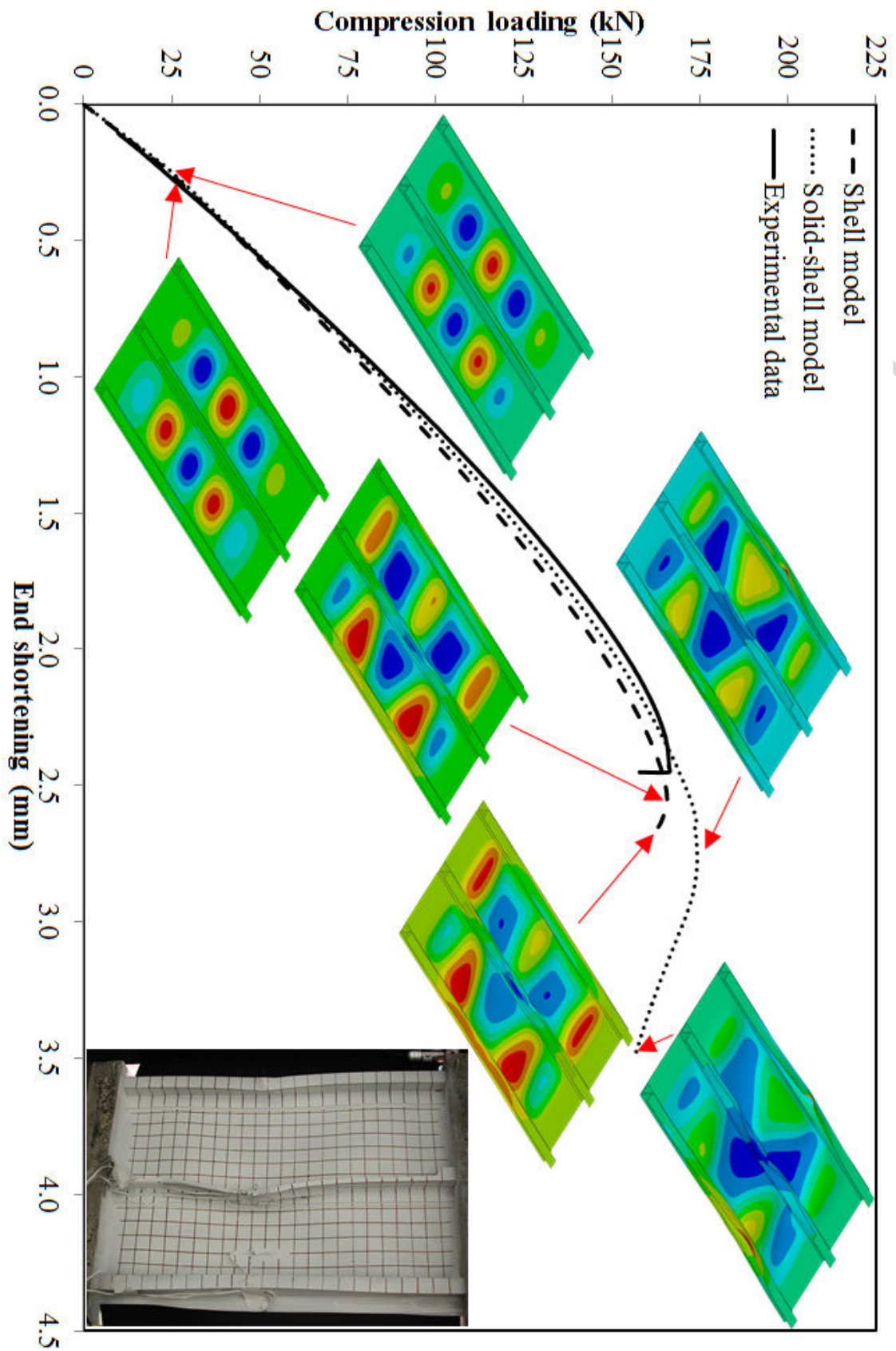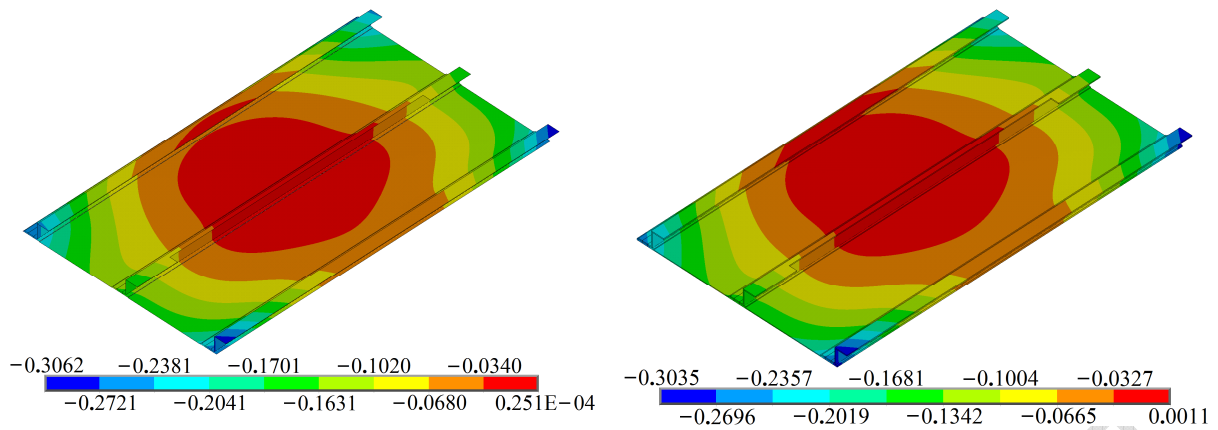
Figure 7. Applied test boundary conditions
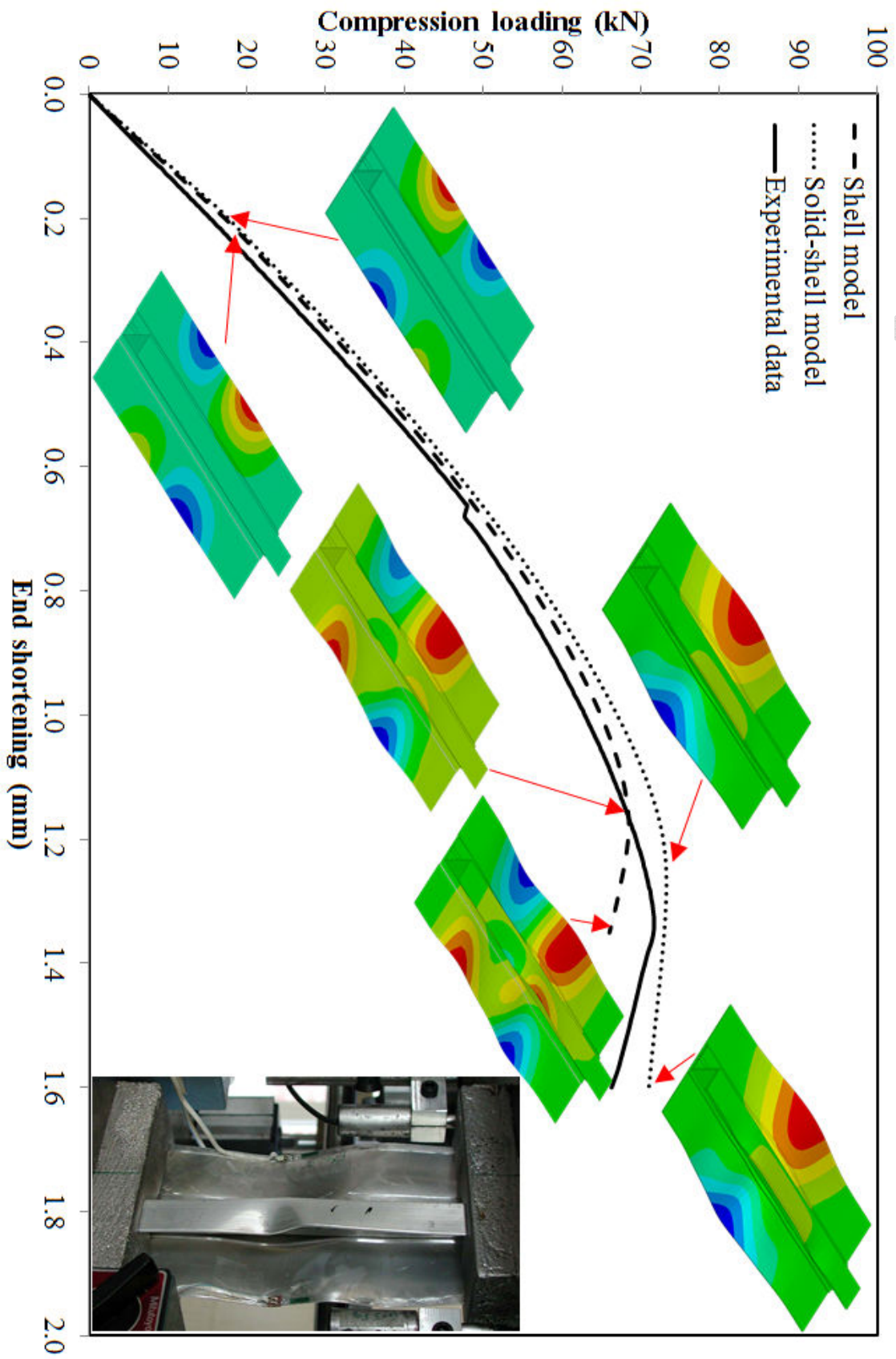
Figure 8. Experimental and predicted load versus end-shortening curves for specimen S1.
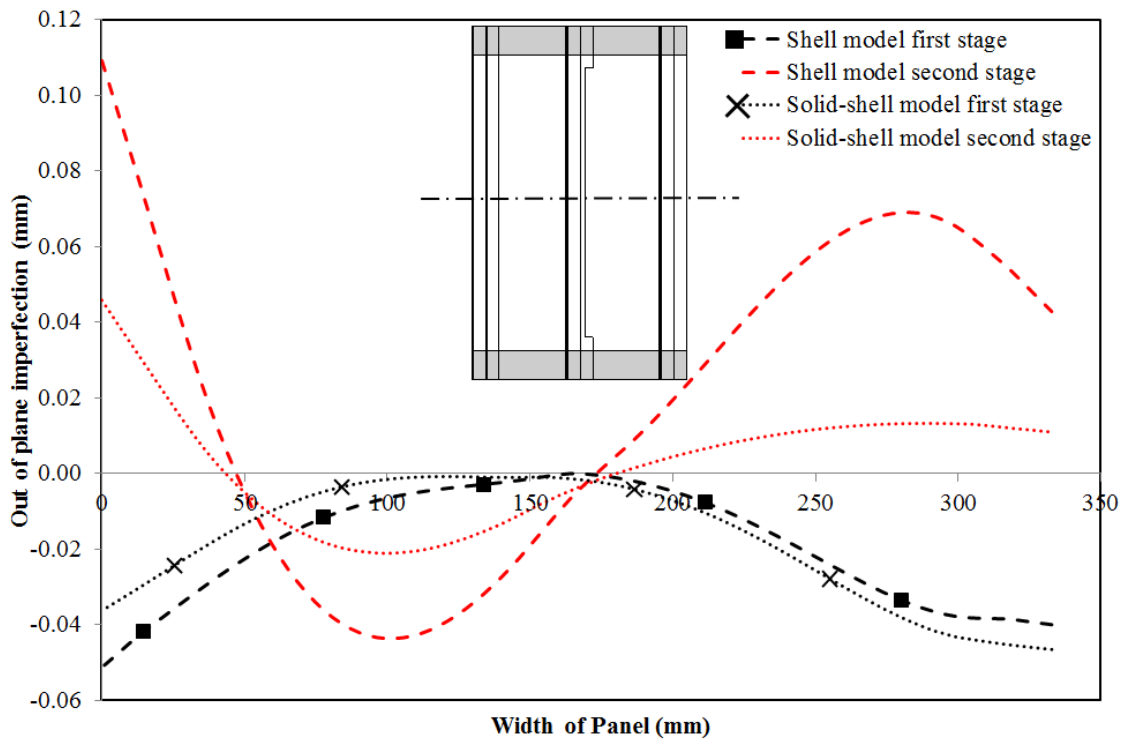
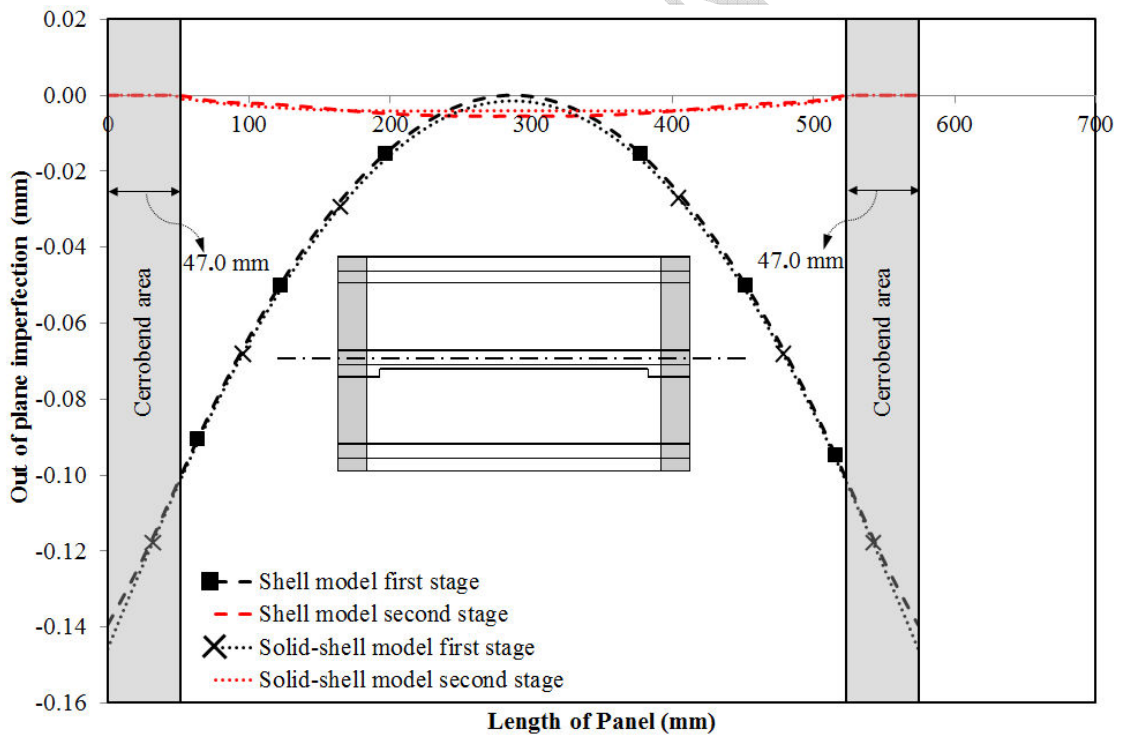a) Shell model   b) Solid-shell model
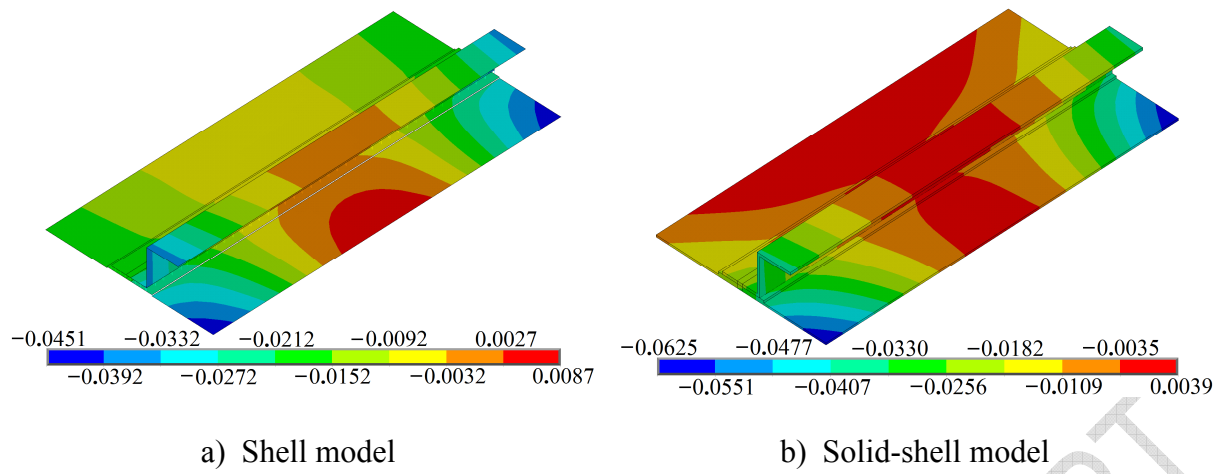
Figure 9. Specimen S1 predicted initial geometric imperfection patterns induced by

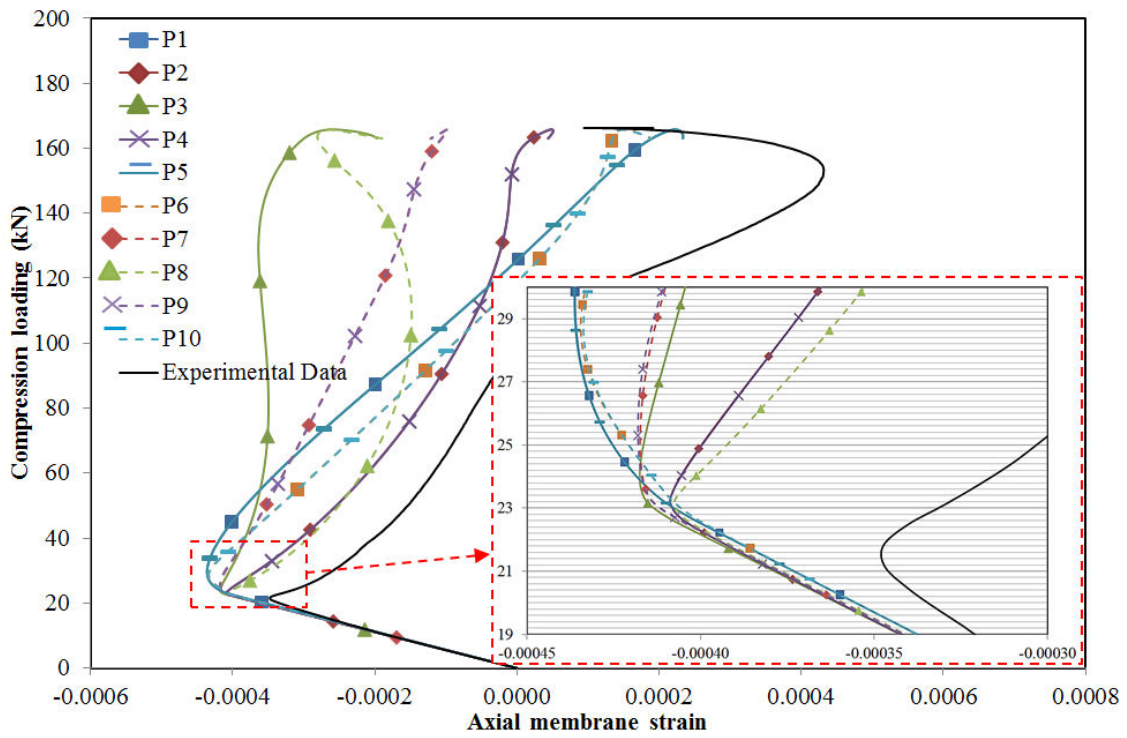modelling the idealised welding residual stress state. (all units in mm)
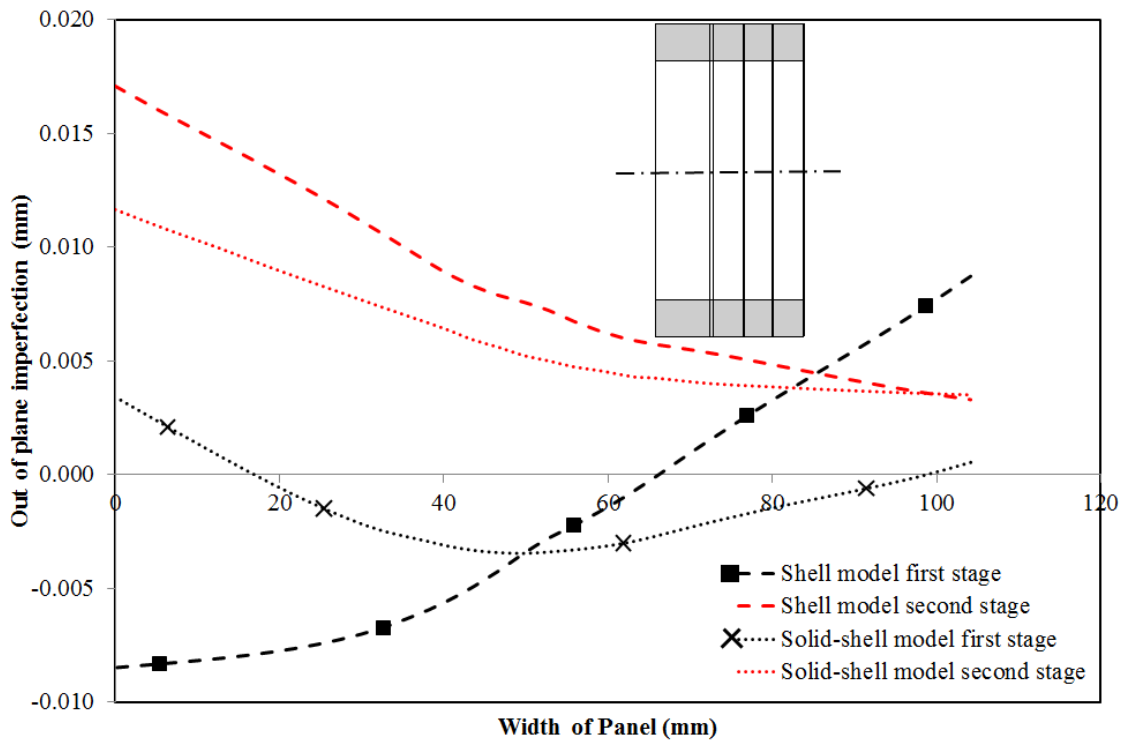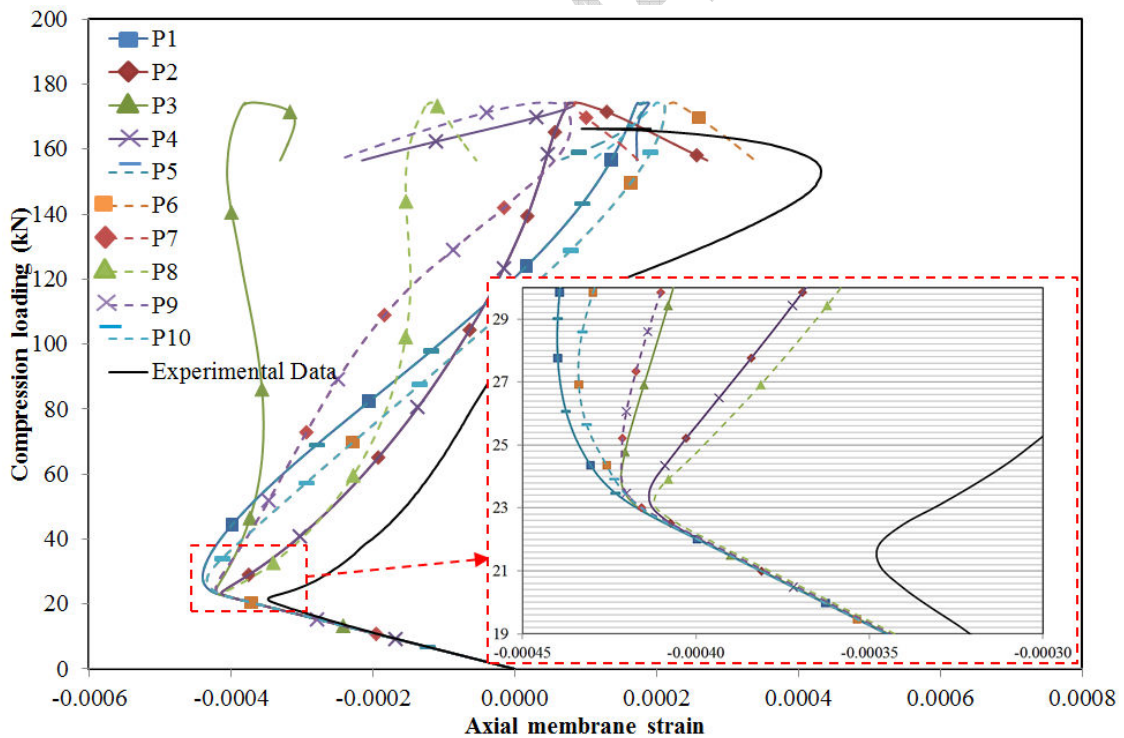
a) Longitudinal mid-length
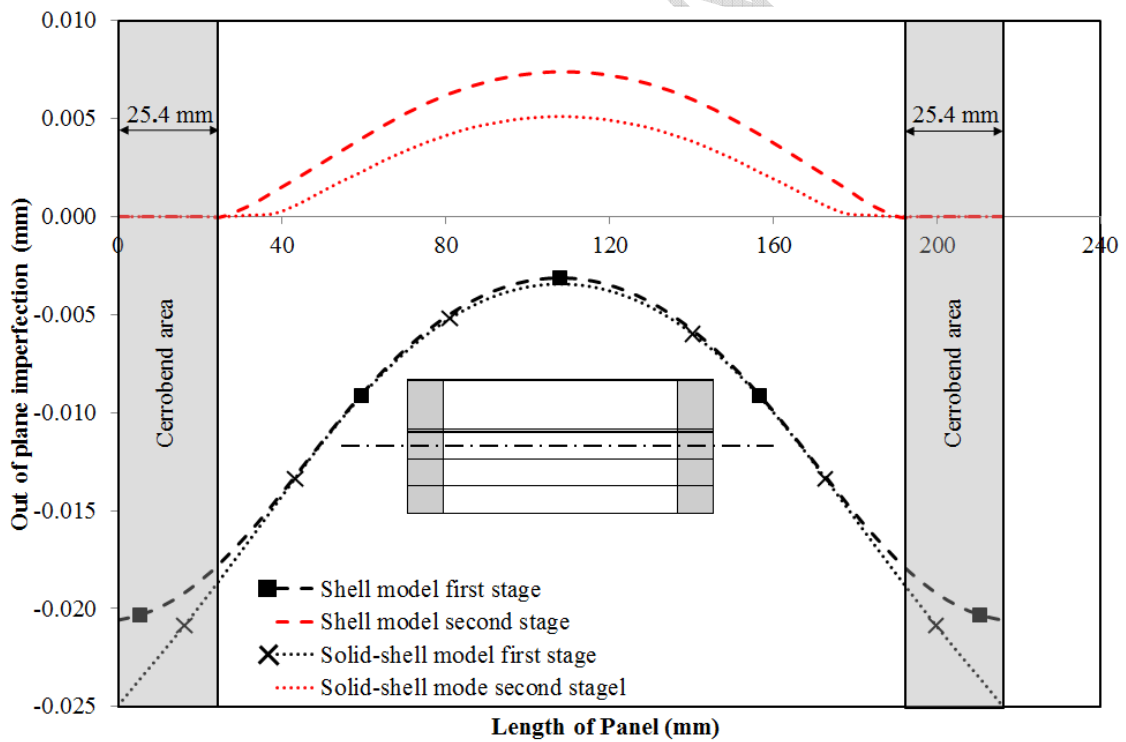
b) Lateral mid-length

Figure 10. Predicted geometric imperfections of specimen S1 with test boundary conditions applied.
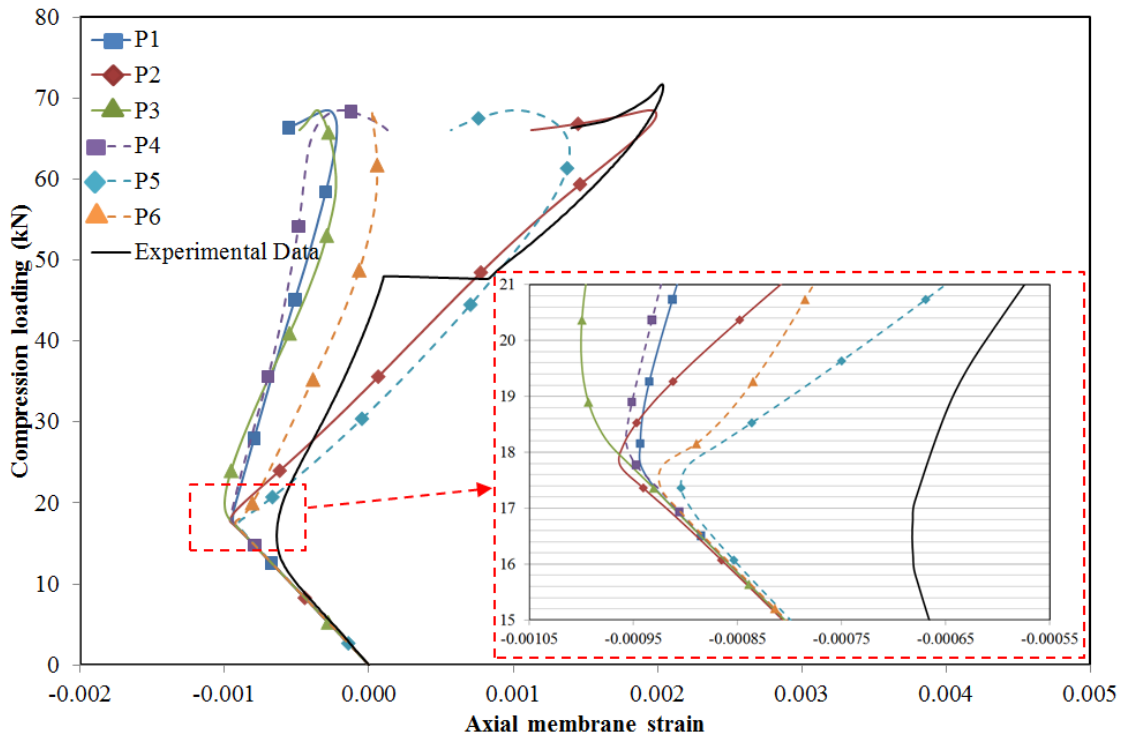
a) Shell model average strain data
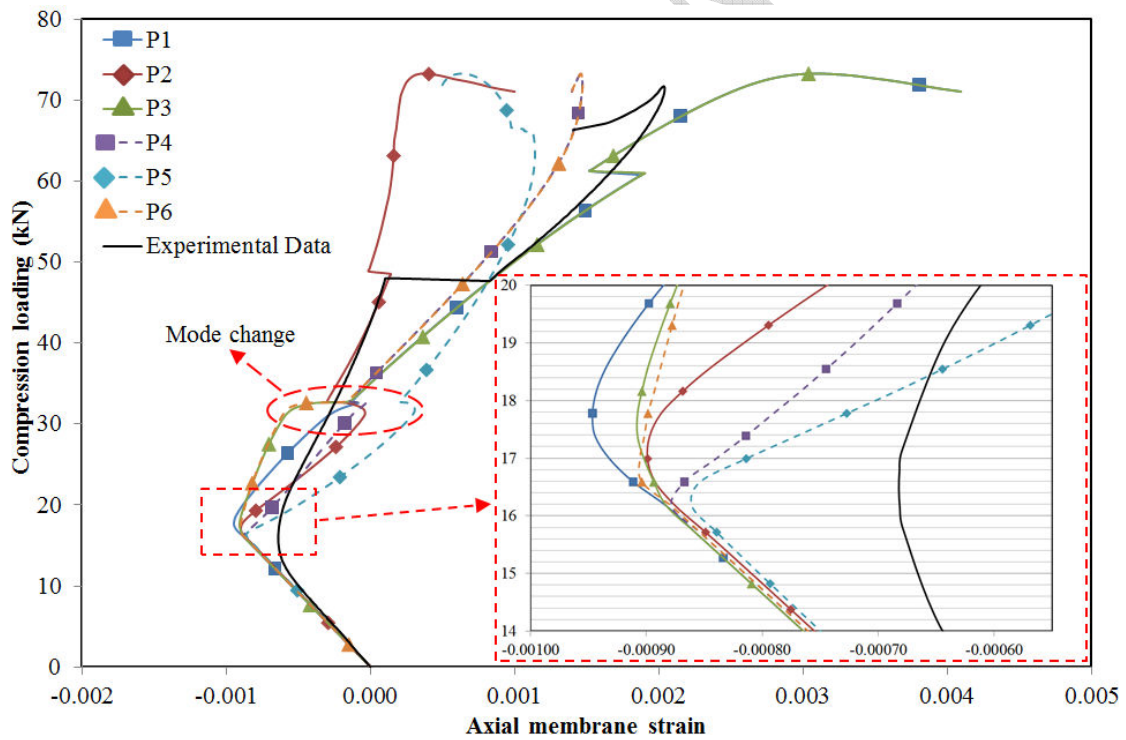
b) Solid-shell model average strain data

Figure 11. Average strain versus load curves for specimen S1.

Figure 12. Boundary condition sensitivity analysis

Figure 13. Experimental and predicted load versus end-shortening curves for specimen S3.

a) Shell model	b) Solid-shell model

Figure 14. Specimen S3 predicted initial geometric imperfection patterns induced by modelling the idealised welding residual stress state. (all units in mm)

a) Longitudinal mid-length

b) Lateral mid-length

Figure 15. Predicted geometric imperfections of specimen S3 with test boundary conditions
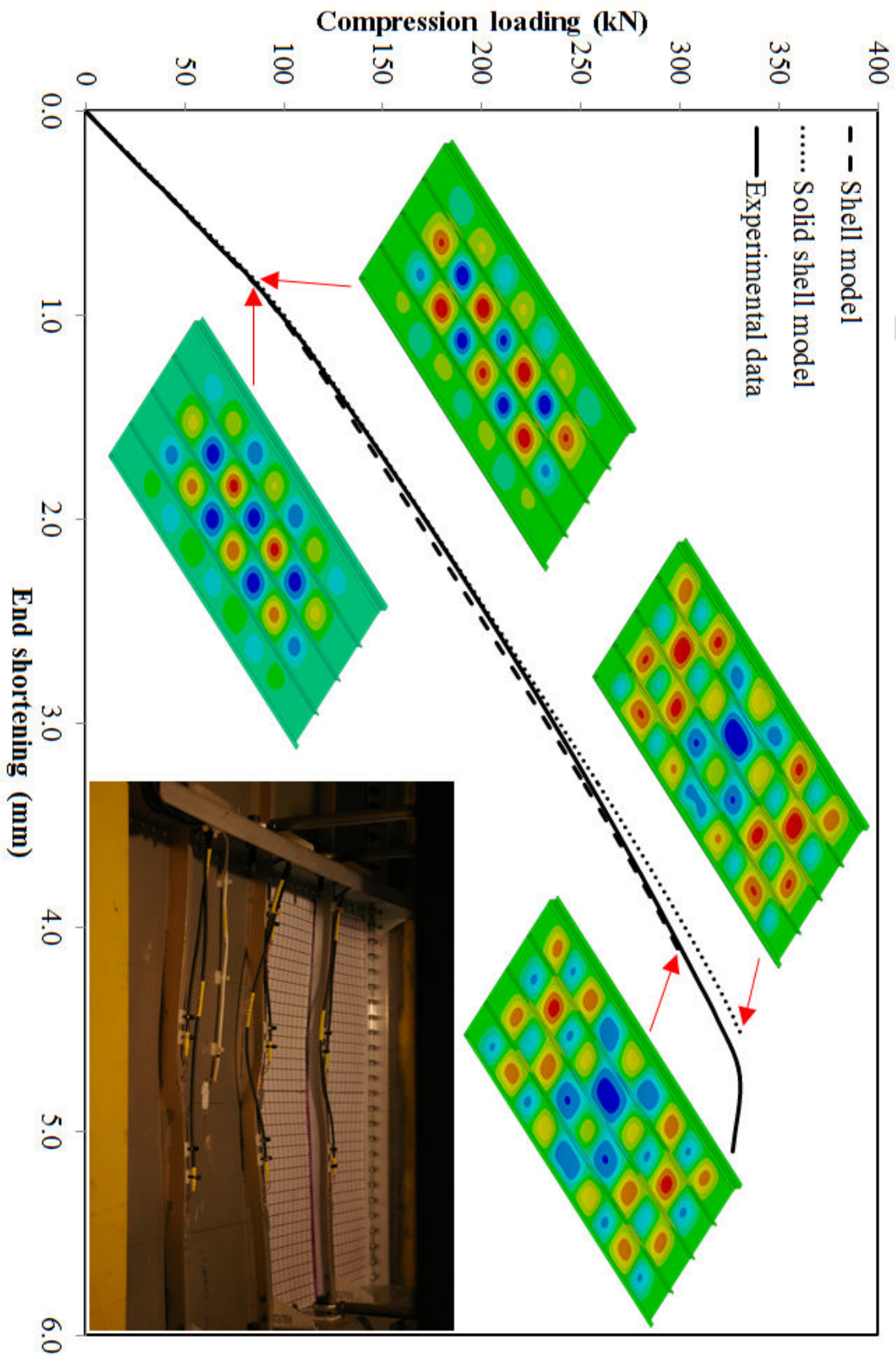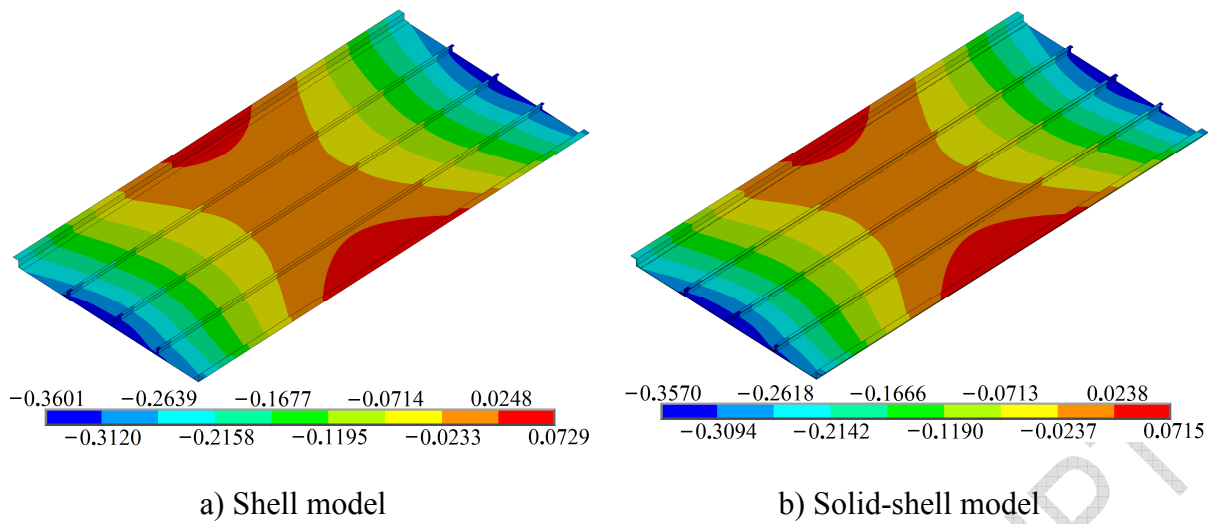
applied.

a) Shell model average strain data

b) Solid-shell model average strain data

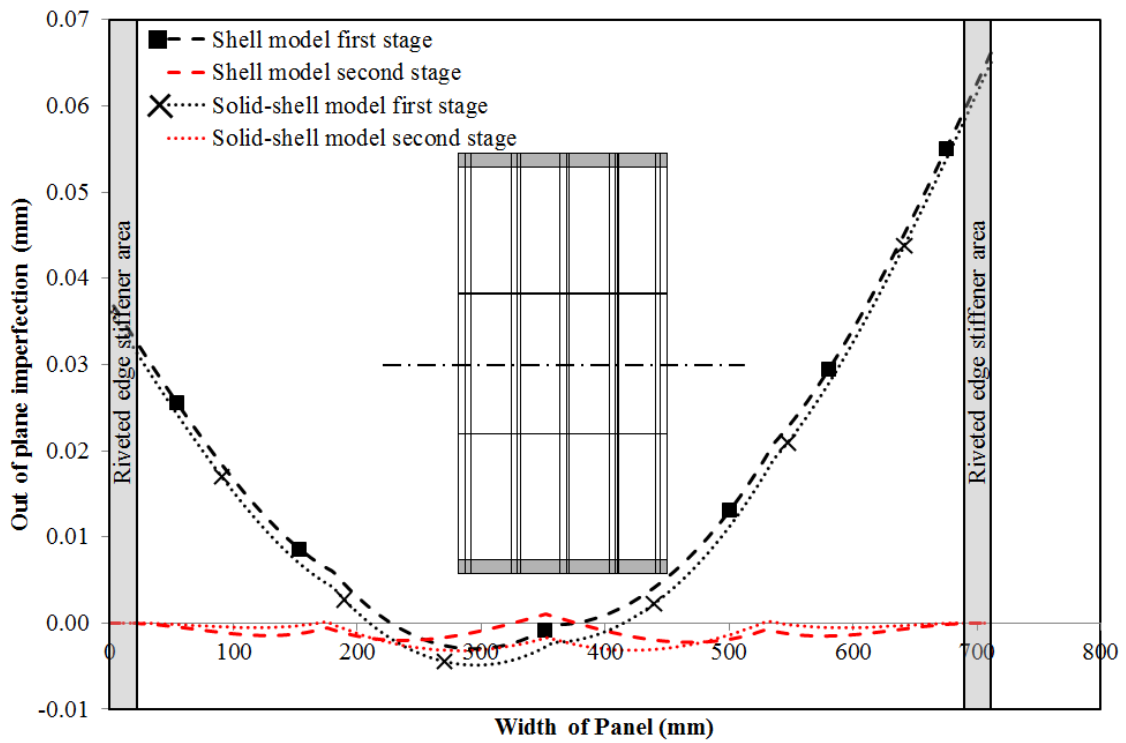**Figure 16.** Average strain versus load curves for specimen S3.

Figure 17. Experimental and predicted load versus end-shortening curves for specimen S7.

a) Shell model   b) Solid-shell model

Figure 18. Specimen S7 predicted initial geometric imperfection patterns induced by

modelling the idealised welding residual stress state. (all units in mm)

a) Longitudinal mid-length

b) Lateral mid-length

Figure 19. Predicted geometric imperfections of specimen S7 with test boundary conditions applied.

a) Shell model average strain data

b) Solid-shell model average strain data

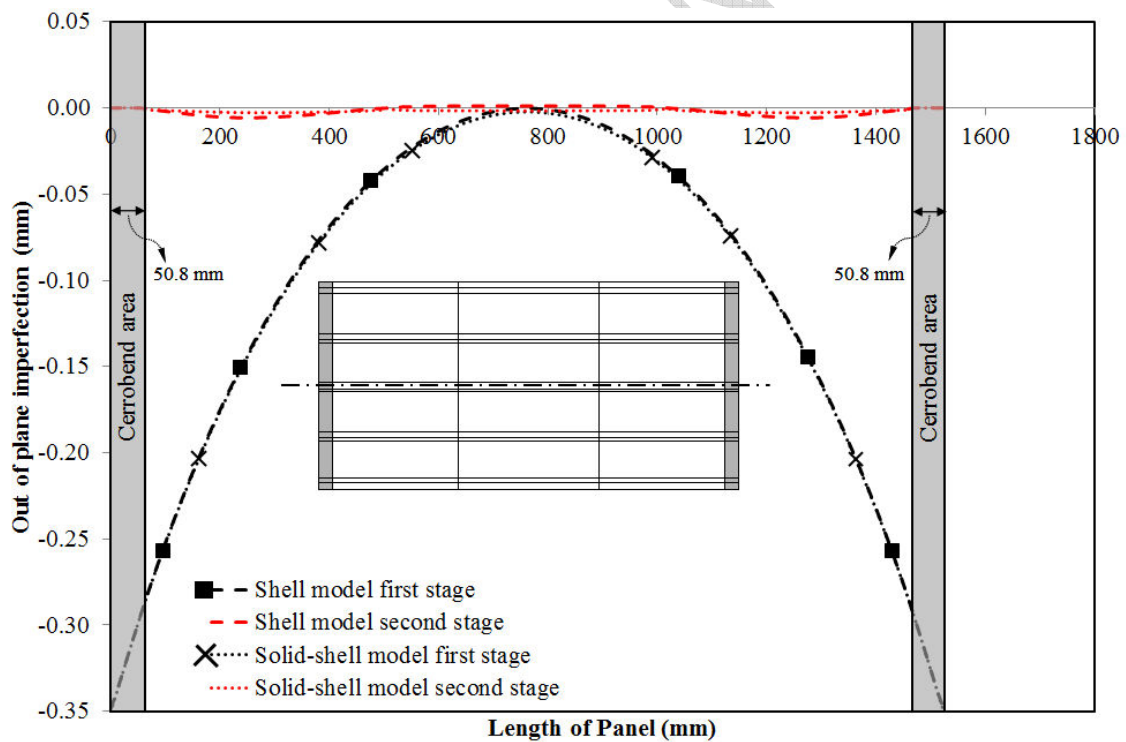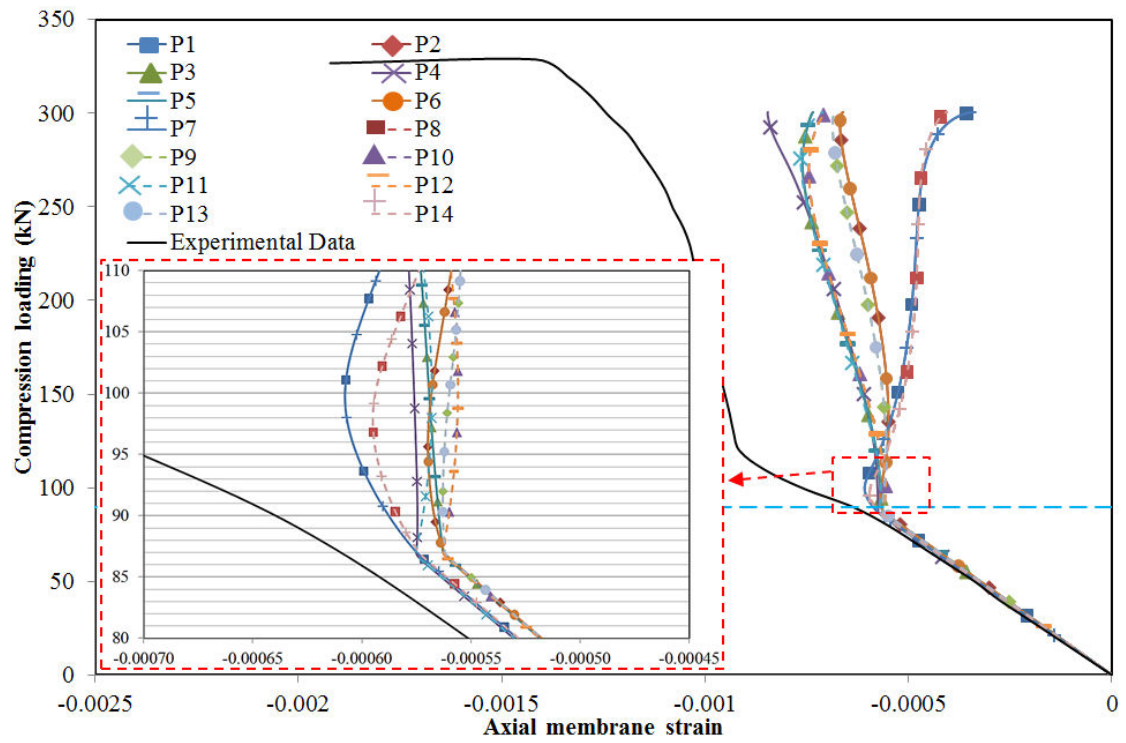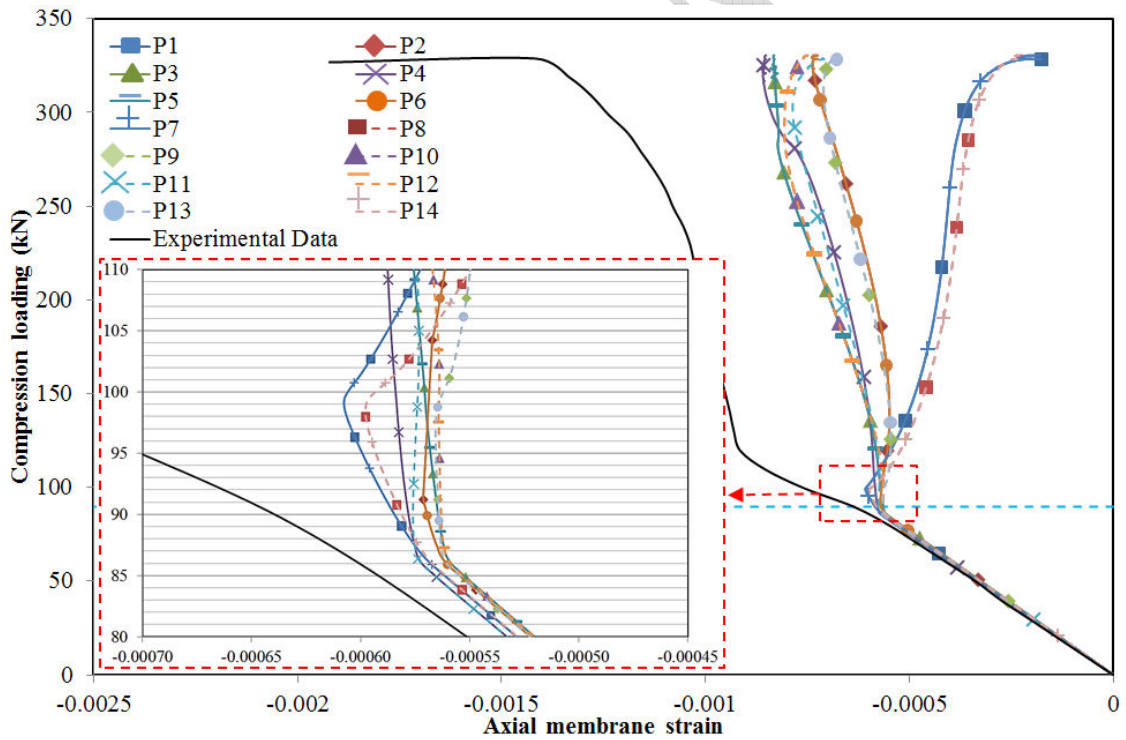**Figure 20.** Average strain versus load curves for specimen S7.

Table 1. Cross sectional dimensions

	Specimen S1	Specimen S3		Specimen S7	
	Stiffener (mm) welded	Edge stiffeners (mm) welded	Central stiffener (mm) welded	Edge stiffeners (mm) riveted	Central stiffeners (mm) welded
h_s	25.4	25.4	25.4	25.4	25.4
b_{ff}	20.32	20.32	7.3	22.86	10.16
b_{af}	22.86	22.86	22.86	20.32	20.32
t_w	1.6	1.6	1.6	3.175	2.032
t_{ff}	1.6	1.6	1.6	3.175	2.032
t_{af}	1.6	1.6	1.6	3.175	2.032
t_{skin}	1.2	1.2		2.032	

Table 2. Specimen residual stress magnitudes and application areas.

Specimen	Longitudinal and lateral tension stress magnitudes plus application area
S1	204.5 MPa are applied to all skin and stiffener elements within 3.048 mm laterally of the weld centre line
S3	204.5 MPa are applied to all skin and stiffener elements within 3.048 mm laterally of the weld centre line
S7	245.4 MPa are applied to all skin and stiffener elements within 2.032 mm laterally of the weld centre line

Table 3. Local skin buckling load results for specimen S1

	Skin local buckling load (kN)				
	Shell181	Solsh190	% difference	a	b
P1	17.9	17.7	1.12	7.83	6.63
P2	17.9	17.1	4.47	7.83	3.01
P3	19.8	17.6	11.11	19.28	6.02
P4	18.2	16.2	10.99	9.64	-2.41
P5	17.5	16.3	6.86	5.42	-1.81
P6	17.6	16.7	5.11	6.02	0.60

[a,b]Percentage differents based on experimental data (16.6 kN) for Shell181 and Solsh190 models

Table 4. Local skin buckling load results specimen S3

	Skin local buckling load (kN)				
	Shell181	Solsh190	% difference	a	b
P1	29.5	28.2	4.41	37.21	31.16
P2	23.2	23.4	-0.86	7.91	8.84
P3	23.9	23.9	0.00	11.16	11.16
P4	23.2	23.4	-0.86	7.91	8.84
P5	29.5	28.2	4.41	37.21	31.16
P6	28.7	27.4	4.53	33.49	27.44
P7	25.5	24.3	4.71	18.60	13.02
P8	23.2	23.2	0.00	7.91	7.91
P9	25.5	24.3	4.71	18.60	13.02
P10	28.7	27.4	4.53	33.49	27.44

[a,b]Percentage differents based on experimental data (21.5 kN) for Shell181 and Solsh190 models

Table 5. Local skin buckling load results for specimen S7

	Skin local buckling load (kN)				
	Shell181	Solsh190	% difference	a	b
P1	100.0	99.0	1.00	11.48	10.37
P2	87.0	86.5	0.57	-3.01	-3.57
P3	87.0	86.5	0.57	-3.01	-3.57
P4	87.0	86.5	0.57	-3.01	-3.57
P5	87.0	86.5	0.57	-3.01	-3.57
P6	87.0	86.5	0.57	-3.01	-3.57
P7	100.0	99.0	1.00	11.48	10.37
P8	98.0	98.5	-0.51	9.25	9.81
P9	87.0	86.5	0.57	-3.01	-3.57
P10	87.0	86.5	0.57	-3.01	-3.57
P11	87.0	86.5	0.57	-3.01	-3.57
P12	87.0	86.5	0.57	-3.01	-3.57
P13	87.0	86.5	0.57	-3.01	-3.57
P14	98.0	98.5	-0.51	9.25	9.81

[a,b]Percentage differents based on experimental data (89.7 kN) for Shell181 and Solsh190 models